

## ABSTRACT

VOOK, TREVOR. Catalytic Graphitization of Biocarbon for Green Battery Anodes. (Under the direction of Dr. William Joe Sagues).

A novel method for the conversion of paper towel waste to graphite anode material is developed and optimized for use in Li-ion batteries. The surge in demand for Li-ion battery anode materials coupled with the unsustainable and highly inefficient methods of producing battery-grade graphite necessitate alternative carbon feedstocks and graphitization technologies. Paper towel waste (PW) is identified as a suitable carbon feedstock for iron-catalyzed graphitization due to its sustainability, low cost, low ash content, and ample supply for the intended end use. A Box Behnken experimental design for statistical optimization is pursued for untreated and pre-carbonized PW with factors of temperature (1100 – 1300°C), hold time (1 – 5 hours), and iron catalyst loading (0.5 – 1.5X fixed carbon content) with graphite crystal size as the primary response variable. Temperature and iron catalyst loading are found to be significant factors, whereas hold time is found to be insignificant. Graphite mass yield, d-spacing, degree of disorder, and extent of graphitization are additional metrics that are assessed to understand biographite quality. Graphitic carbon morphologies typical of those reported in steel refining, including spheres, platelets, and cones, are observed. The reversible capacities of the untreated and pre-carbonized biographite anodes are calculated to be 355 and 340 mAh g<sup>-1</sup>, respectively, which are highly competitive with commercial Li-ion anodes. The main advantages of using untreated PW appears to be higher quality graphite, the requirement for relatively lower temperatures with shorter hold times, and greater Li-ion battery performance, while the disadvantages are a less uniform graphite product and potentially poor commercial viability due to the necessity for a large graphitization reactor.

© Copyright 2022 by Trevor Vook

All Rights Reserved

Catalytic Graphitization of Biocarbon for Green Battery Anodes

by  
Trevor Vook

A thesis submitted to the Graduate Faculty of  
North Carolina State University  
in partial fulfillment of the  
requirements for the degree of  
Master of Science

Biological and Agricultural Engineering

Raleigh, North Carolina  
2022

APPROVED BY:

---

Dr. William Joe Sagues  
Committee Chair

---

Dr. Praveen Kolar

---

Dr. Sunky Park

---

Dr. Afsaneh Rabiei

## **DEDICATION**

This work is dedicated to my grandparents Allen, Lois, Frederick, and Frederica for their encouragement to pursue graduate studies. This work is also dedicated to my parents Lisa and Eric Vook.

## **BIOGRAPHY**

Trevor Vook was born in Chapel Hill and raised in Durham, NC. Trevor was active in Boy Scouts and earned the rank of Eagle Scout in 2017. He attended North Carolina State University from 2017 to 2020 graduating with a Bachelor's of Science in mechanical engineering. Trevor interned for Clearwater Paper Corporation and Tower Engineering Professionals while an undergraduate student. In the summer of 2020, Trevor applied to and was accepted into the Biological and Agricultural Engineering Masters of Science program and Dr. William Joe Sagues hired him as a graduate research assistant. Trevor presented virtually at the 2021 ASABE Annual International Meeting and won an award for his presentation. Trevor also won second place in a two minute presentation competition hosted by the College of Agriculture and Life Sciences in the fall of 2021. Upon graduation, he plans to pursue an engineering job in Raleigh.

## ACKNOWLEDGMENTS

I want to thank Dr. Dan Harris, Dr. Praveen Kolar, Dr. Sunkyu Park, Dr. Afsaneh Rabiei, Dr. Mark Nimlos (NREL), Dr. Sang-Don Han (NREL), Dr. Jennifer Forrester, Dr. Steven Hall, Dr. Garey Fox, Dr. Christopher Winkler, Chuck Mooney, Lisa Lentz, Eliezer Reyes Molina, Ethan Woods, Shaikat Chandra Dey and most of all Dr. William Joe Sagues for their support and instruction throughout my graduate studies at NC State.

### Research Statements:

This work was performed in part at the Analytical Instrumentation Facility (AIF) at North Carolina State University, which is supported by the State of North Carolina and the National Science Foundation (award number ECCS-1542015). This work made use of instrumentation at AIF acquired with support from the National Science Foundation (DMR-1726294). The AIF is a member of the North Carolina Research Triangle Nanotechnology Network (RTNN), a site in the National Nanotechnology Coordinated Infrastructure (NNCI).

This work was performed in part at the Environmental and Agricultural Testing Service Laboratory (EATS), Department of Crop and Soil Sciences, at North Carolina State University.

## TABLE OF CONTENTS

LIST OF TABLES .....	vi
LIST OF FIGURES .....	vii
<b>1.1 Introduction</b> .....	1
<b>1.2 Experimental Methods</b> .....	7
1.2.1 Materials .....	7
1.2.2 Design of Experiments.....	8
1.2.3 Catalytic Graphitization.....	9
1.2.4 Acid Washing.....	9
1.2.5 X-ray Diffraction .....	10
1.2.6 Raman Spectroscopy.....	11
1.2.7 Scanning Electron Microscopy & Electron Dispersive X-ray Spectroscopy .....	11
1.2.8 Transmission Electron Spectroscopy.....	12
1.2.9 Elemental Analysis .....	12
1.2.10 Thermogravimetric Analysis .....	13
1.2.11 Electrochemical Testing.....	13
<b>1.3 Results &amp; Discussion</b> .....	14
1.3.1 Graphitization Factors.....	15
1.3.2 Mass Balance .....	29
1.3.3 Biographite Morphology.....	32
1.3.4 Lithium-Ion Cell Performance .....	35
<b>1.4 Conclusions</b> .....	39
<b>References</b> .....	44

## LIST OF TABLES

Table 1.1	Experimental Design Effects.....	8
Table 1.2	Graphite Crystal Size, Mass Yield, D-spacing, and Degree of Disorder .....	16
Table 1.3	Maximum and Minimum Crystal Size, Mass Yield, and D-Spacing.....	18
Table 1.4	Maximum and Minimum Crystal Size and Degree of Disorder Comparison.....	24
Table 1.5	Results from the statistical analysis that was conducted to identify the significance or insignificance of various factors and combinations of factors for biographite crystal size .....	25
Table 1.6	Optimal conditions for maximum crystal size and corresponding predicted and actual crystal size .....	28
Table 1.7	Mass Composition.....	30

## LIST OF FIGURES

Figure 1.1	Response surface plots with biographite crystal size on z-axis and temperature, catalyst loading, and time on x-axes .....	19
Figure 1.2	Response surface plots with biographite mass yield on z-axis and temperature, catalyst loading, and time on x-axes .....	21
Figure 1.3	Response surface plots with biographite d-spacing on z-axis and temperature, catalyst loading, and time on x-axes .....	23
Figure 1.4	X-ray diffractograms of commercial graphite, optimal pre-carbonized biographite, and optimal untreated biographite .....	26
Figure 1.5	Rama spectra for A) untreated and B) pre-carbonized biographite .....	27
Figure 1.6	Statistical model prediction profiles for A) untreated and B) pre-carbonized .....	28
Figure 1.7	Mass balances for untreated (top) and pre-carbonized (bottom) paper waste .....	31
Figure 1.8	SEM Images of Untreated PW, EDS Images of Untreated Graphite with Iron, and Untreated Graphite SEM .....	33
Figure 1.9	SEM Images of Pre-carbonized PW, EDS Images of Graphite with Iron, and SEM Images of Pre-carbonized Graphite .....	34
Figure 1.10	TEM Image of Untreated Graphite .....	35
Figure 1.11	Electrochemical performance of bio graphites (from paper towel waste): (a) galvanostatic discharge and charge profiles, (b) cycling stability plot (commercial graphite for comparisons) (at C/10 in the voltage range of 0.005 - 1.5 V), and (c) Rate capability plot (at varying c-rate in the voltage range of 0.005 - 1.5 V).....	38

## 1.1 Introduction

The demand for lithium-ion batteries is projected to increase by 30% yearly until 2030 and one of the limiting components of this battery production is high quality graphite for the anode, costing \$10 to \$20 per kg<sup>1</sup>. Many countries including the United States have no automotive-grade graphite production capabilities even though graphite is identified as a critical raw material, which puts strain on global supply chains<sup>2-5</sup>. The supply chain of graphite and other material components has the potential to confuse benefits of electrification<sup>6</sup>. Graphite is a crystalline allotrope of carbon, composed of stacked sheets between which Li ions can be inserted reversibly<sup>7,8</sup>. Currently, battery-grade graphite is produced through mining and purification of natural graphite or conversion of high quality petroleum distillate bottoms into synthetic graphite<sup>3</sup>. Both of these processes are resource intensive. Mining and processing of natural graphite requires energy-intensive ore extraction and mechanical separation and flotation, followed by toxic hydrofluoric acid purification<sup>5,9</sup>. Producing synthetic graphite from petroleum involves treatment temperatures of ~3000°C and reaction times of multiple days to even weeks, resulting in significant energy consumption and carbon emission with 30 to 40% of the mass is converted to greenhouse gases<sup>10,11</sup>. Batteries for residential or grid storage used in conjunction with renewable energy can have significant economic and environmental benefits such as those seen with Tesla's Powerwall system<sup>12,13</sup>. There is also at the same time a large shift in the automobile industry towards electric vehicles which will further strain this material<sup>14,15</sup>. Reducing the cost and environmental impact of graphite production, while not sacrificing performance, would improve battery production as a whole<sup>16</sup>.

A sustainable and economical graphite production process must be developed to utilize a variety of biocarbon feedstocks, because nearly 85% of the world's graphite is produced in a few

countries<sup>3</sup>. Biomass generally does not graphitize when heated to high temperatures (~3000°C) under inert environments and requires a catalyst, unlike most fossil based carbon resources<sup>17</sup>. Carbon fibers from lignin have shown an inability to graphitize with the same quality as commercial fibers and contain disordered regions<sup>18</sup>. Recently, researchers have overcome this barrier by developing catalytic methods to produce graphite from biocarbon, allowing for significantly lower temperatures of operation relative to traditional operations using fossil carbon<sup>19</sup>. Sagues et al. (2020) identified that softwood performs the best out of various feedstocks for catalytic graphite production<sup>20</sup>. They also found that low silica and ash content are desirable to make better quality graphite. Graphite with smaller particle size has been found to have higher capacity but reduced thermal stability which could be at play given the elongated shape of various biomass feedstocks<sup>21</sup>. Using an iron catalyst is ideal due to its relative abundance and potential to incorporate this process with other industrial manufacturing<sup>22</sup>.

Paper towel waste is an abundant, low silica, and low ash feedstock. In 2018, the United States produced 3.79 million tons of tissue paper and towels produced<sup>23</sup>. The United states imported around 44,000 tons of graphite in 2018, due to not having domestic graphite mines<sup>24</sup>. If only 1.2% of the paper tissue and towel mass produced was converted into graphite it could cover the United States' domestic needs. There is a large amount of tissue that is used for sanitary purposes or soiled in an extreme manner and would not be conducive for graphitization, but only around 10% of the tissue and towel would be required to enter the graphitization process. The waste from professional institutions where there are trash cans adjacent to a paper towel bin is almost free from contaminants other than trace soap and oils. The water would be removed via evaporation and fully removed in a drying process. Currently a majority of paper towel waste is still sent to the landfill with a steady increase in composting the paper towels.

Composting is much better because it reduces the use of lined landfill volume. There has been some investigation comparing the life cycle of air dryers versus paper towel dispensers and they found it was heavily dependent on the carbon intensity of the electricity running the hand dryer<sup>25</sup>. Joseph et al. (2015) compared the 30 second use of a hand dryer to the use of two paper towel sheets to dry hands and found that there was less overall environmental impact from air dryers, including composting the paper towel. This LCA was performed with composting paper waste while a large portion of paper waste is still landfilled. Other value added processes have been investigated including hydrogen gas production through fermentation and also producing levulinic acid as another mechanism of valorization<sup>26,27</sup>. There has been significant investigation into the proper mechanism for hand drying and there is not a conclusive preferred method for hygienic reasons<sup>28</sup>.

Thompson et al. (2015) was one of the first groups to report a method for producing graphite from biocarbon using iron as a catalyst<sup>29</sup>. They identified the challenge of controlling porosity and graphite content, which both impact use as an energy storage material. They overcame this challenge by modifying the iron to biomass ratio, which tuned the porosity without changing graphite content. This article includes high quality scanning electron micrographs of the graphite crystal structure. For their experimental setup, softwood sawdust and iron nitrate were mixed in an aqueous solution prior to air drying. Next, they placed the sample into a furnace flushed with N<sub>2</sub> and heated it smoothly to the maximum temperature of 800°C. Finally, they used HCl to remove iron from the samples and DI water mixed with ethanol to complete the purification. They performed XRD and Raman to assess graphite quality. They addressed the idea that a technology cannot be seen as an environmentally preferred option until all of the effects and costs are described. Life cycle analysis is one key piece missing from many

research studies in this area. Although Thompson et al. (2015) made an impactful contribution to the field of biocarbon graphitization, their biographite products were not tested in lithium-ion cells and thus potential benefits on the energy storage industry were not illuminated.

Wheat stalk was selected by Zhou et al. (2016) as a viable feedstock for graphitization after hydrothermal treatment<sup>30</sup>. Their highly graphitic nanosheets (HGNS) performed better than multiple other carbon-based battery anodes at high current rates with a capacity of 161.4 mA h g<sup>-1</sup> at 10C. Their 0.5 C reversible capacity is reported to be 486.9 mA h g<sup>-1</sup>. They found that their HGCNS production process resulted in a yield of 11.3% from the initial wheat stalk<sup>30</sup>

It is clear that lithium ion batteries have a critical use in our society, but there is much room for improvement in the manufacturing process. Banek et al. (2018) innovated a breakthrough in the production of graphite from biocarbon, which has the potential to dramatically change the environmental impact of lithium ion battery production<sup>31</sup>. They developed a 2-step graphitization process, with step 1 involving pyrolysis of biocarbon at 600°C to create biochar, and step 2 involving laser ablation of the biochar to generate highly crystalline graphite. This process was thought to be transferrable to a wide variety of biomaterial, which would otherwise be of lesser value. Banek et al. (2018) identified this process as being carbon negative as the carbon within the process becomes captured in the graphite lattice and not released as gas; LCA was not performed to validate this claim. This process has been developed and performed at an experimental scale and more research will be involved in scaling-up this process to industrial quantities.

Gomez-Martin et al. (2018) performed graphitization of low cost biomass and varied the maximum pyrolysis temperature from 850 to 2000°C to analyze the effects of crystallinity and the microstructure on anodic capabilities<sup>32</sup>. They used an iron catalyst and nitric acid etching to

purify the carbon. They discovered for a few trials an initial charging capacity of  $\sim 500 \text{ mA h g}^{-1}$ , which quickly reduced to below  $320 \text{ mA h g}^{-1}$ . Gomez-Martin et al. (2019) furthered their research by using a nickel catalyst to synthesize graphene sheets from biomass<sup>33</sup>. Their electrochemical testing revealed subpar results but were satisfied with the simplicity and sustainability of this process.

Bamboo wood, German wood, and petroleum coke reference material were all graphitized at temperatures ranging from  $800^\circ\text{C}$  to  $2800^\circ\text{C}$  showing an increase in electrochemical performance and carbon content as the temperature was increased in that range<sup>34</sup>. Fromm et al. (2018) did not pursue catalytic graphitization out of concerns about the remaining catalyst from experiments graphitizing using various catalyst elements at high temperatures and with phenolic resin carbon<sup>35</sup>.

Various biomass feedstocks have been proposed as precursors to catalytic graphitization. Xia et al. (2020) selected a variety of forest residue biomass including chestnut shells, bamboo, poplar, cotton stalk, Jatropha shell, and lotus<sup>36</sup>. They confirmed the potential for using agricultural and forestry waste residue for graphitization. They discovered that porosity and degree of graphitization were affected by temperature and the iron catalyst loading used. They were limited in their temperature range and their highest operating temperature was  $800^\circ\text{C}$  and resulted in poor graphitization, indicating higher ideal temperatures.

Sagues et al. (2020) performed catalytic graphitization of all their feedstocks with a 30 weight percentage iron powder catalyst loading<sup>20</sup>. Their baseline procedure involved heating the biocarbon/iron mixtures from 25 to  $600^\circ\text{C}$  at a rate of  $3^\circ\text{C}$  per minute, and then from 600 to  $1200^\circ\text{C}$  the ramp increased to  $10^\circ\text{C}$  per minute. They also performed a fast experiment where the heat ramp stayed at  $10^\circ\text{C}$  per minute for the entire temperature range and a hold experiment (the

baseline) held at 1200°C for an hour before shutoff. The furnace was under a constant flow of nitrogen to prevent oxidation and to remove any volatiles. Sagues et al. (2020) separated the graphite from the added iron catalyst via hydrochloric acid reflux. XRD and Raman spectroscopy were performed on the resulting graphitic material. They created scanning electron microscope and transmission electron microscope images to further qualify the graphitic structure. The iron catalyst melted into a liquid and was able to penetrate the feedstock through the cellular pores. Sagues et al. (2020) determined that in softwood the graphitization was catalyzed to a greater degree than for hardwood. In the Kraft lignin the iron catalyst did not melt and stayed in its initial shape. Graphitized softwood was selected as the most promising feedstock and electrochemical tests were performed showing this as a viable anode material.

Waste coffee grounds were carbonized to form a hard carbon anode material and tested electrochemically showing some promise as a waste anode material<sup>37</sup>. Hong et al. (2021) found a reversible capacity of 100 mA h g<sup>-1</sup> at a rate of 2C which is low compared to other commercial samples, but is functional as anode material. This study does not use a catalyst and only goes to a process temperature of 800°C in carbonization resulting in no graphitic structure and thus we see poor electrochemical performance. This is an interesting study because it shows a biomass anode material production process that has some measure of success.

There is a potential to make a high value product from the paper towel waste which will sequester the carbon within the final graphite. Research has been performed creating hierarchical porous carbon from paper towel waste using potassium hydroxide<sup>38</sup>. This porous carbon was used as an adsorbent of harmful tetracycline antibiotics from the environment. This hard carbon was much lower quality than graphite which was okay because for its purposes it still could

perform as well as needed. This study does confirm the ability to use paper towel waste as a feedstock in a conversion process to create a value added carbon product.

The specific objectives of this project are to verify paper towel waste as a graphite feedstock, quantify effects on crystal size of various factors, and investigate the properties of graphite that is produced. This project will include necessary experiments to create high quality graphite. This objective has been tentatively met through initial testing identifying graphite. Box Behnken experimental designs will be performed with temperature, peak hold time, and iron catalyst loading as the factors to determine the effects of each on crystal size. There will be two independent experiments, one will have non-carbonized paper towel waste and the other will undergo a carbonization process prior to graphitization. Electrochemical battery testing will be performed to determine the electrochemical properties of the graphite. Scanning electron microscopy (SEM) is performed to verify the physical features of the produced graphite and compare with commercial standards. Initial testing indicates that time has a lesser effect than temperature and catalyst loading. This graphite is expected to perform above or at commercial standards based on XRD testing. The carbonized paper towel waste is expected to perform better and more consistently than the untreated waste.

## **1.2 Experimental Methods**

### **1.2.1 Materials**

Scott KCO1000 Recycled bleached paper towels were dispensed and used to dry hands, simulating typical use. This paper towel waste was then placed in a 105°C oven to dry. The dried paper towels are then ground in an IKA cutting and grinding mill. The paper towels are ground until they pass through a final 0.1mm sieve upon exiting the mill which will homogenize the

feedstock. This paper towel powder is stored in the laboratory and dried again in the 105 °C oven prior to weighing and use in experiment runs.

Preparation of the carbonized paper towel waste feedstock was performed by heating the paper towel waste up to 1000°C at a 5°C min<sup>-1</sup> heating and cooling rate under nitrogen (200 mL/min). The fixed carbon percentage of dried paper towel waste was determined to be 18.25% which was used as the basis for iron catalyst ratio in experiments.

### 1.2.2 Design of Experiments

Box Behnken statistical design of experiments approach was used to create two separate sets of experiments for the catalytic graphitization of untreated paper towel waste and carbonized paper towel waste. In this design, three factors are varied at three levels. Maximum temperature values are 1100°C, 1200°C, and 1300°C. Hold time at the maximum temperature is set at 1, 3, and 5 hours. Iron catalyst loading is set at 0.5, 1, and 1.5 as a ratio of the iron mass to the mass of fixed carbon in the feedstock. In this experimental design a relatively high iron catalyst loading is acceptable due to the low cost, earth abundant, and non-toxic nature of iron powder<sup>22</sup>. Iron is also a steel manufacturing byproduct and there is potential to integrate graphite production with that process. For the pre-carbonized experimental design this ratio will be between the iron and the mass of carbonized paper towel waste. The Box Behnken design creates set points for the three variables at specific combinations of their levels in order to quantify the variable effects.

**Table 1.1:** *Experimental Design Effects*

Factor	Name	Units	[-1]	[0]	[1]
A	Temperature	°C	1100	1200	1300
B	Hold Time	hours	1	3	5
C	Iron Loading	X FC	0.5	1	1.5

There were 17 experiments in both designs, which included 5 center points [000]. The graphite crystal size was the response variable and fit in a statistical model (JMP) to determine maximal settings for the three input variables. For this experiment p-values less than 0.05 were considered significant, p-values less than 0.10 were considered moderately significant with larger values not considered significant. For a certain factor, the p-value shows the likelihood that the observed results are seen if the null hypothesis was true. Smaller p-values correspond with the alternative hypothesis having greater evidence. After the initial experiments were performed, a model was fit and then subsequent experiments at both the untreated and carbonized maximum conditions were performed.

### **1.2.3 Catalytic Graphitization**

Catalytic graphitization was performed using PW with commercial iron powder ( $<10\mu\text{m}$ ) used as the catalyst. The stock iron container was only opened in nitrogen atmosphere to prevent oxidation. The correct amount of dried PW or carbonized PW was measured out and the corresponding iron catalyst was weighed. The PW and catalyst were then mixed thoroughly before being pressed into an alumina crucible. The crucible was then inserted into a tube furnace and the furnace was sealed. Nitrogen gas then purges the tube furnace of air and is steadily flowing throughout the experiment. The furnace was then programmed to ramp from room temperature to the maximum temperature at  $5^\circ\text{C min}^{-1}$  and then hold for the specified time before cooling to room temperature at  $5^\circ\text{C min}^{-1}$ .

### **1.2.4 Acid Washing**

The graphite and iron catalyst mixture was removed from the crucible and weighed. Hydrochloric acid reflux was then used to remove iron from the sample. A 2.5 wt% loading of graphite was combined with hydrochloric acid (37%) and left to heat and boil for three hours<sup>20</sup>.

The heat was then turned off and the round bottom flask was filled with deionized water. This was allowed to cool and sit overnight. The iron chloride, hydrochloric acid, and deionized water was removed through vacuum filtration and the graphite was rinsed with additional deionized water (1L). This purification process was modeled after Sagues et. al<sup>20</sup>.

### 1.2.5 X-ray diffraction

X-ray diffraction was performed using a PANalytical Empyrean X-ray diffractometer outfitted with a copper anode. Diffraction was scanned at 0.026261 degree intervals. The diffraction patterns were analyzed using Line-Profile Analysis Software (LIPRAS) and the Scherrer equation was used to estimate the graphite crystal size.

LIPRAS is a software tool that was developed for analysis of powder diffraction data through peak fitting with various functions<sup>39</sup>. There is a MATLAB plugin version of LIPRAS in addition to a stand-alone package which is what this research used. Data was opened in LIPRAS and the range was set between 20-30 degrees 2-theta. The baseline was established with points at 20, 21, 29, and 30 degrees 2-theta and then an Asymmetric Pearson VII peak shape function was used to model the peak. All of the other primary peak-shape functions resulted in a less consistent fit of our data. LIPRAS outputs peak position and halfway height peak width, among other data, which is then used in the subsequent analysis.

The Scherrer equation is used to quantify the size of the crystal structure, wherein L is the crystal size, K is a shape factor constant,  $\lambda$  is the X-ray wavelength, B is the width of the main peak at the halfway height, and  $\theta$  is the Bragg angle of the beam:

$$L = \frac{K\lambda}{B\cos(\theta)} \quad (1)$$

Bragg's law is used to calculate interatomic spacing of the crystalline planes in the graphite which is referred to as d-spacing. Equation 2 is used to calculate the d-spacing where  $n$  is diffraction order,  $\lambda$  is the X-ray wavelength, and  $\theta$  is the Bragg angle of the beam:

$$d - \text{spacing} = \frac{n\lambda}{2\sin(\theta)} \quad (2)$$

A new metric was created for this study, termed the "Degree of Disorder" (DoD), which is used to estimate the degree to which a biographite sample is disordered carbon. The DoD is calculated by taking the ratio of background intensity (BGI) with baseline intensity (BLI), wherein the BGI is the background intensity at 2-theta of 20 degrees and BLI is the baseline intensity after 2-theta of 30 degrees. The DoD relationship is shown in equation 3.

$$DoD = \frac{BGI}{BLI} \quad (3)$$

### 1.2.6 Raman Spectroscopy

Raman spectra was captured at ten different locations on our sample using a Horiba XploRA PLUS Confocal Raman Microscope. The sample was placed onto a sample stage and the microscope was focused on each location for scanning.

$$\alpha = \frac{I(G)}{I(D) + I(G)} \quad (4)$$

Equation 4 was used to determine the extent of graphitization  $\alpha$  from the intensity of the D and G peaks which are represented by  $I(D)$  and  $I(G)$  respectively. The extent of graphitization was calculated for each spectra and then averaged. The standard deviation of the extent of graphitization was also calculated from the different locations.

### 1.2.7 Scanning electron microscopy & electron dispersive X-ray spectroscopy

A small amount of the sample was sprinkled onto carbon tape attached to standard 12.5mm aluminum pin mount sample stubs. The sample stage was then inserted into a Hitachi

SU3900 Scanning Electron Microscope. SEM images were taken with a 20 KeV beam with backscattered electron composition in a traditional backscatter setting. Custom backscattered electron images were also taken with one element off and a side element on to see shadow and sample texture. X-ray data was collected with an Oxford Ultimex 40 Silicon Drift X-ray Detector. All images were taken in variable pressure mode with 30 Pa dry nitrogen vacuum.

### **1.2.8 Transmission electron microscopy**

A Thermo Fisher Talos F200X G2 Transmission Electron Microscope (TEM) instrument with a 200 kV Field Emission Gun (FEG) was used to analyze samples. The samples were deposited onto a thin TEM grid and inserted into the instrument for analysis.

### **1.2.9 Elemental analysis**

Elemental analysis was performed on the acidic liquid rinsate, PW powders, and Graphite using a Perkin Elmer 8000 Inductively-coupled plasma-Optical Emission Spectrometer (ICP-OES). The acid wash rinsate was diluted and then analyzed in the ICP-OES for iron content. The powders were digested with a wet digestion procedure based on an EPA method<sup>40</sup>. The samples were first weighed into a capped digestion tube and 10 ml of 5N nitric acid was added. They were left overnight to predigest. The next day they were mixed while heating for 15 minutes. After they cooled, 10 ml of concentrated nitric acid was added and they were then heated for 2 hours. After cooling again, 1-2 ml of 30% hydrogen peroxide was added and the sample allowed to effervesce, then heated up and, cooled. The hydrogen peroxide addition and heating process was repeated until a total of 6 ml was added. At this point the cap is removed and the sample is heated for 2-3 hours or until it reaches 5-8 ml of volume. Once cooled, 1 ml of concentrated hydrochloric acid is added and the samples are heated for 40 minutes. They are cooled again and distilled water is added before filtration. The filtered sample is then run on the ICP-OES.

Carbon analysis was performed with a LECO 928 CN Macro Determinator. A weighed sample is placed in the ceramic boat which is then inserted into a high temperature horizontal ceramic combustion furnace. The sample is combusted under oxygen at high temperature and combustion gasses are extracted from the furnace through a thermoelectric cooler and allowed to equilibrate in a ballast volume. The gas is then extracted and combined with a stream of inert gas to pass under a non-dispersive infrared (NDIR) cell which detects carbon dioxide and provides the carbon content of the sample.

#### **1.2.10 Thermogravimetric Analysis**

Thermogravimetric Analysis (TGA) was performed on the PW feedstock, carbonized PW, and graphite samples using a TA Instruments Q500 Thermogravimetric Analyzer. Roughly 11 to 12 mg of sample was placed into the sample holder and heated up to 800 C with a 10 C/min heating rate in an atmosphere of N<sub>2</sub>. The sample was held at the peak temperature of 800 C for 10 minutes, then the atmosphere was changed to oxygen and held for another 10 minutes at the same temperature in order to oxidize the remaining carbon and leave only the ash content of the sample. Following the 10 minutes of air purge, the data collection was ended.

#### **1.2.11 Electrode Preparation, Cell Fabrication and Electrochemical Testing**

Biographite electrodes are prepared from slurry with the following composition: active material (85 wt.%), Super C45 carbon black (5 wt.%, Timcal) as conductive additive, and PVdF (polyvinylidenedifluoride) binder (10 wt.%, Solvay) mixture with N-methyl-2-pyrrolidone (NMP) solvent. This slurry is pasted onto Cu-foil current collector and dried at 120 °C for 12 h under vacuum. Electrodes with a diameter of 14 mm are punched, and the average active material loading density is 4.9 mg cm<sup>-2</sup>. The electrochemical performance of the prepared electrodes is evaluated using CR2032 coin-type cells assembled in an Ar-filled glove box. Li

metal is used as a counter and reference electrode, and a solution of 1.2 M lithium hexafluorophosphate ( $\text{LiPF}_6$ ) in ethylene carbonate (EC):ethylmethylcarbonate (EMC) (3 : 7 wt.%) (Gen II electrolyte) is employed as the electrolyte. Galvanostatic discharge/charge tests are performed in a range of 0.005 to 1.5 V (vs.  $\text{Li}/\text{Li}^+$ , hereafter) at a variety C-rate (1 C corresponded to about  $350 \text{ mA g}^{-1}$ ).

### 1.3 Results & Discussion

The primary aim of this study was to understand the feasibility of catalytically graphitizing paper towel waste for use in lithium-ion battery anodes. Specifically, this study set out to achieve the following objectives:

1. Identify advantages and disadvantages to pre-carbonizing the PW prior to graphitization
2. Elucidate the effects of various factors including temperature, time, and catalyst loading
3. Quantify the mass balance for the catalytic graphitization process
4. Observe and compare graphite morphologies to those reported in steel manufacturing
5. Assess electrochemical performance and compare with commercial lithium-ion cells
6. Identify areas for improvement in future work

For objectives 1 & 2, graphite crystal size as measured via XRD was the primary metric used for benchmarking and comparison. For objective 3, a series of analytical techniques, including electron dispersive X-ray spectroscopy, inductively-coupled plasma-optical emission spectrometry, and thermogravimetric analysis, were used to quantify the various mass flows

throughout the process. For objective 4, scanning electron microscopy and transmission electron microscopy were used to detect and assess the different graphitic carbon morphologies. For Objective 5, the biographite products were used in the construction of lithium-ion half cells for galvanostatic discharge and charge cycling. Objective 6 is accomplished by recognizing further opportunities in this research topic.

### **1.3.1 Graphitization Factors**

Box Behnken statistical optimization models with three factors and three levels were used to investigate differences between untreated and pre-carbonized PW and elucidate effects of the various factors, thereby satisfying Objectives 1 & 2. Table 1.2 contains the various combinations of levels and factors that were assessed per the Box Behnken design. Conditions are designated as combinations of symbols -, 0, +, where – represents the minimum level for a particular factor, 0 represents the baseline level for a particular factor, and + represents the maximum level of a particular factor. Herein, the order of factors is as follows: temperature, hold time, and catalyst loading. For example: (- + 0) indicates -1 temperature (1100°C), +1 hold time (5h), and 0 catalyst loading (1.0X fixed carbon). The resultant crystal size, mass yield, and d-spacing from the Box Behnken experiments are also shown in Table 1.2. The crystal size for a reference commercial graphite was measured to be 181.28 Angstroms, and thus this was the intended target. Notably, the crystal sizes obtained from the PW were not significantly close in value to the commercial reference, but the electrochemical performance from the biographite was competitive with commercial graphite anodes, as will be discussed in subsequent sections. D-spacing is the distance between graphitic sheets in the biographite materials and, like crystal size, is another important metric for understanding graphite quality. The commercial graphite reference material has a d-spacing of 3.36 Angstroms, which is the ideal distance for Li-ion intercalation and

diffusion.<sup>41</sup> As can be seen in Table 1.2, the conditions with low crystal size also have large d-spacing, thereby making them inadequate for Li-ion intercalation. The center point (0,0,0) replicates show good reproducibility with standard deviations of 1.61 and 3.52 angstroms for untreated and pre-carbonized graphite, respectively.

**Table 1.2:** Graphite Crystal Size, Mass Yield, D-spacing, and Degree of Disorder

Treatments				Untreated Graphite				Pre-Carbonized Graphite			
Conditions	Temperature	Hold Time	Catalyst Loading	Crystal Size (Angstroms)	Mass yield (%)	d-spacing (Angstroms)	DoD	Crystal Size (Angstroms)	Mass yield (%)	d-spacing (Angstroms)	DoD
--0	-1	-1	0	35.85	14.10	3.41	1.34	46.79	15.16	3.40	1.53
-+0	-1	1	0	53.7	14.71	3.40	1.62	66.79	13.03	3.38	1.86
+0	1	-1	0	77.46	14.97	3.38	1.06	65.23	12.39	3.38	1.11
++0	1	1	0	81.4	14.46	3.38	0.85	66.51	11.46	3.38	1.09
0--	0	-1	-1	69.52	13.88	3.39	1.08	58.87	12.83	3.39	1.46
0+-	0	-1	1	91.05	13.91	3.37	0.92	68.72	12.68	3.38	1.41
0+-	0	1	-1	73.04	13.89	3.39	1.15	67.12	14.04	3.38	1.09
0++	0	1	1	79.58	14.15	3.38	0.80	69.8	12.37	3.38	1.10
-0-	-1	0	-1	33.06	14.76	3.50	2.34	43.73	13.01	3.37	2.06
+0-	1	0	-1	74.19	13.54	3.39	1.12	59.56	12.46	3.39	1.04
-0+	-1	0	1	47.83	13.48	3.39	1.65	64.17	12.85	3.37	2.24
+0+	1	0	1	88.36	13.77	3.38	0.86	85.27	11.49	3.38	1.09
000	0	0	0	84.66	14.07	3.38	0.73	65.83	12.88	3.38	1.16
000	0	0	0	82.4	13.15	3.37	1.14	63.96	11.95	3.38	1.10
000	0	0	0	84.16	14.53	3.38	0.68	71.57	14.45	3.38	1.03
000	0	0	0	82.18	14.61	3.38	0.76	70.3	13.95	3.38	1.10
000	0	0	0	80.13	11.58	3.38	1.09	73.29	14.21	3.38	1.04

To better understand pertinent data, the maximum and minimum values and corresponding conditions for crystal size, mass yield, and d-spacing are shown in Table 1.3 and response surface plots are shown in Figures 1.1-1.3. The crystal sizes for untreated biographite range from 33.06 (-1, 0, -1) to 91.05 (0, -1, 1) Angstroms and for pre-carbonized biographite from 43.73 (-1, 0, -1) to 85.27 (1, 0, 1) Angstroms. Thus, the range of crystal size values is larger for untreated biographite, which could be due to the enhanced reactivity between the iron catalyst and the volatile mass in the untreated PW. Untreated PW generated a maximum graphite crystal size of ~91.05 angstroms, which was 5.7 angstroms larger than the maximum

graphite crystal size obtained from the pre-carbonized PW. For both untreated and pre-carbonized PW, the maximum crystal size was obtained with a +1 catalyst loading. Notably, the maximum crystal size for untreated PW was achieved with a 0 temperature and -1 time, whereas that for pre-carbonized PW was achieved with a +1 temperature and 0 time. Thus, based on an initial assessment of the data, the pre-carbonized PW appears to require higher temperature and more time to generate a graphite crystal size of comparable size to that for untreated PW. For both untreated and pre-carbonized PW, the minimum crystal sizes were obtained with -1 temperature and -1 catalyst loading, thereby demonstrating the importance of high temperatures and catalyst loadings and relative unimportance of time. The biographite mass yields for untreated PW range from 11.46% (1, 1, 0) to 15.16% (-1, -1, 0) and for pre-carbonized PW from 11.58% (0, 0, 0) to 14.97% (1, -1, 0). For both untreated and pre-carbonized PW, the maximum yields were obtained with -1 hold time, thereby demonstrating that mass is continuously lost with time at the operating temperature, albeit not to a great extent. The minimum d-spacing for both untreated and pre-carbonized PW is approximately 3.37 angstroms, which is suitable for lithium-ion intercalation. The maximum d-spacing for untreated PW biographite (3.499 angstroms) is significantly higher than that for pre-carbonized biographite (3.397 angstroms) and not suitable for lithium-ion intercalation. The range in d-spacing for untreated PW is much greater than that for pre-carbonized, which follows the same trend observed for crystal size.

**Table 1.3: Maximum and Minimum Crystal Size, Mass Yield, and D-Spacing**

		Untreated		Pre-carbonized	
		Value	Condition	Value	Condition
Crystal Size (angstroms)	Max.	91.05	0, -1, 1	85.27	1, 0, 1
	Min.	33.06	-1, 0, -1	43.73	-1, 0, -1
Mass Yield (%)	Max.	14.97	1, -1, 0	15.16	-1, -1, 0
	Min.	11.58	0, 0, 0	11.46	1, 1, 0
d-Spacing (angstroms)	Max.	3.49943	-1, 0, -1	3.39660	-1, -1, 0
	Min.	3.36970	0, 0, 0	3.37008	-1, 0, 1

As shown in Figure 1.1, response surface plots were generated to visualize the relationship between biographite crystal size and temperature, catalyst loading, and time. For both untreated and pre-carbonized PW, low temperature and low catalyst loading resulted in low crystal size, indicated by the sharp red minimums shown in plots 1.1A+C. Notably, pre-carbonized PW appears to require high temperature and catalyst loading to achieve maximum crystal size, indicated by the sharp blue maximum in plot 1.1C, whereas untreated PW requires moderate temperature and catalyst loading, indicated by the broad, flat blue maximum in plot 1.1A. Thus, future work should investigate a broader range of levels with higher temperatures and catalyst loadings, since it appears that further gains in crystal size are possible. For both untreated and pre-carbonized PW, time seems to be insignificant at higher temperatures, and moderately significant at lower temperatures, indicated by the flat, broad blue maximum for all time points in plots 1.1B+D. Thus, future work should investigate longer hold times at lower temperature to see if graphite crystal sizes comparable to high temperature, lower time treatments are possible.

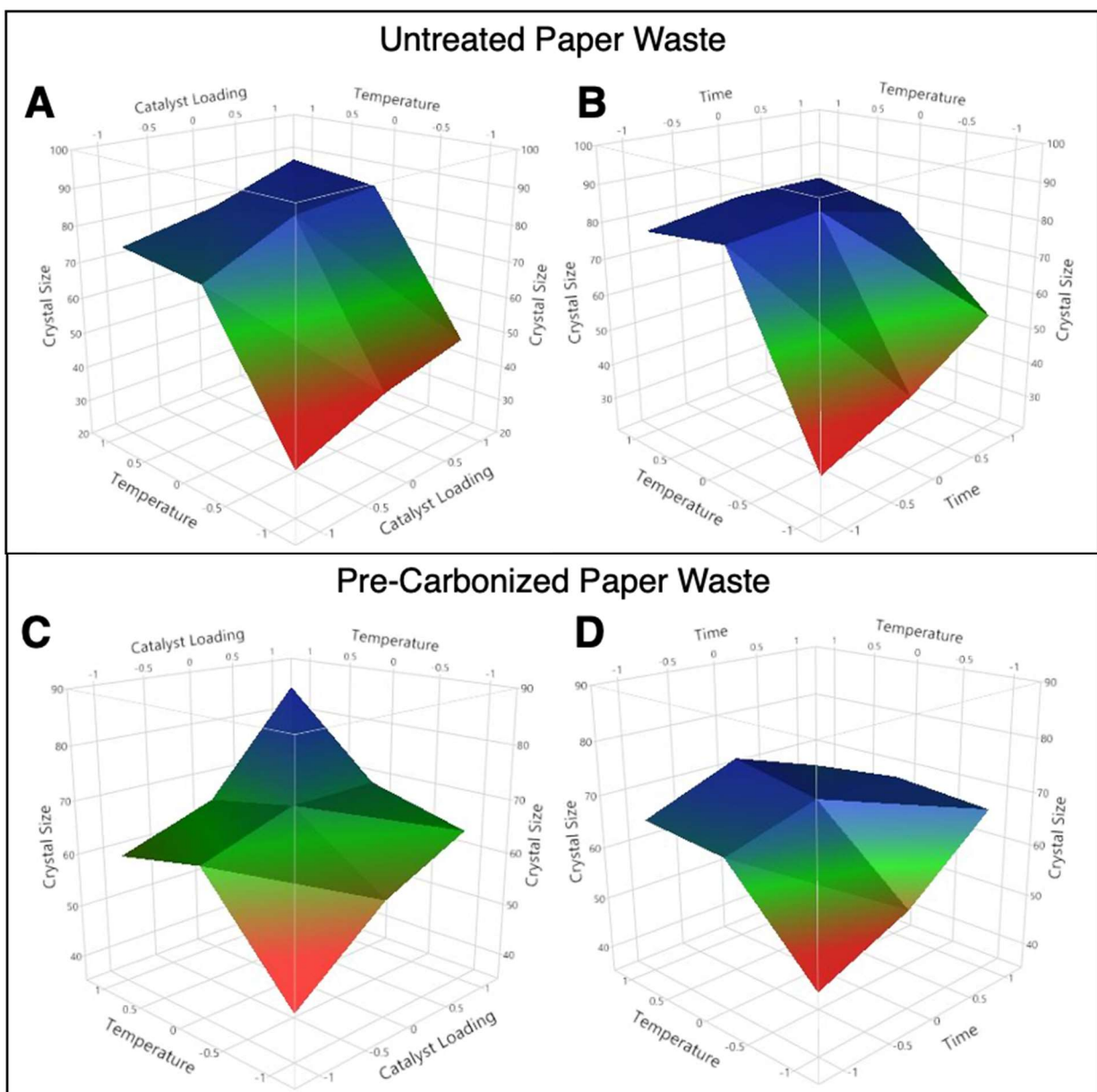


**Figure 1.1:** Response surface plots with biographite crystal size on z-axis and temperature, catalyst loading, and time on x-axes. A) untreated PW biographite crystal size with variation in temperature and catalyst loading B) untreated PW biographite crystal size with variation in temperature and time, C) pre-carbonized PW biographite crystal size with variation in temperature and catalyst loading, D) pre-carbonized PW biographite crystal size with variation in temperature and time.

As shown in Figure 1.2, response surface plots were generated to visualize the relationship between biographite mass yield and temperature, catalyst loading, and time. Notably, the overall geometries of the response surface plots vary substantially between untreated and pre-carbonized PW feedstocks. For the untreated PW shown in plots 1.2A+B, depressed regions near center points are observed, indicating a complex relationship with mass yield and temperature, catalyst loading, and time. It was apparent that low temperatures resulted in higher mass yields. For untreated PW, the overall fluctuation in mass yields was relatively small, and thus the complex relationships were deemed relatively unimportant. For the pre-carbonized PW shown in plots 1.2C+D, trends are more apparent than for the untreated PW. Specifically, lower temperatures and catalyst loadings clearly resulted in higher mass yields for pre-carbonized PW. However, like with crystal size, time did not seem to play an important role. Notably, high mass yields were generally accompanied with lower graphite crystal size, and thus high mass yield does not automatically indicate a more techno-economic process.

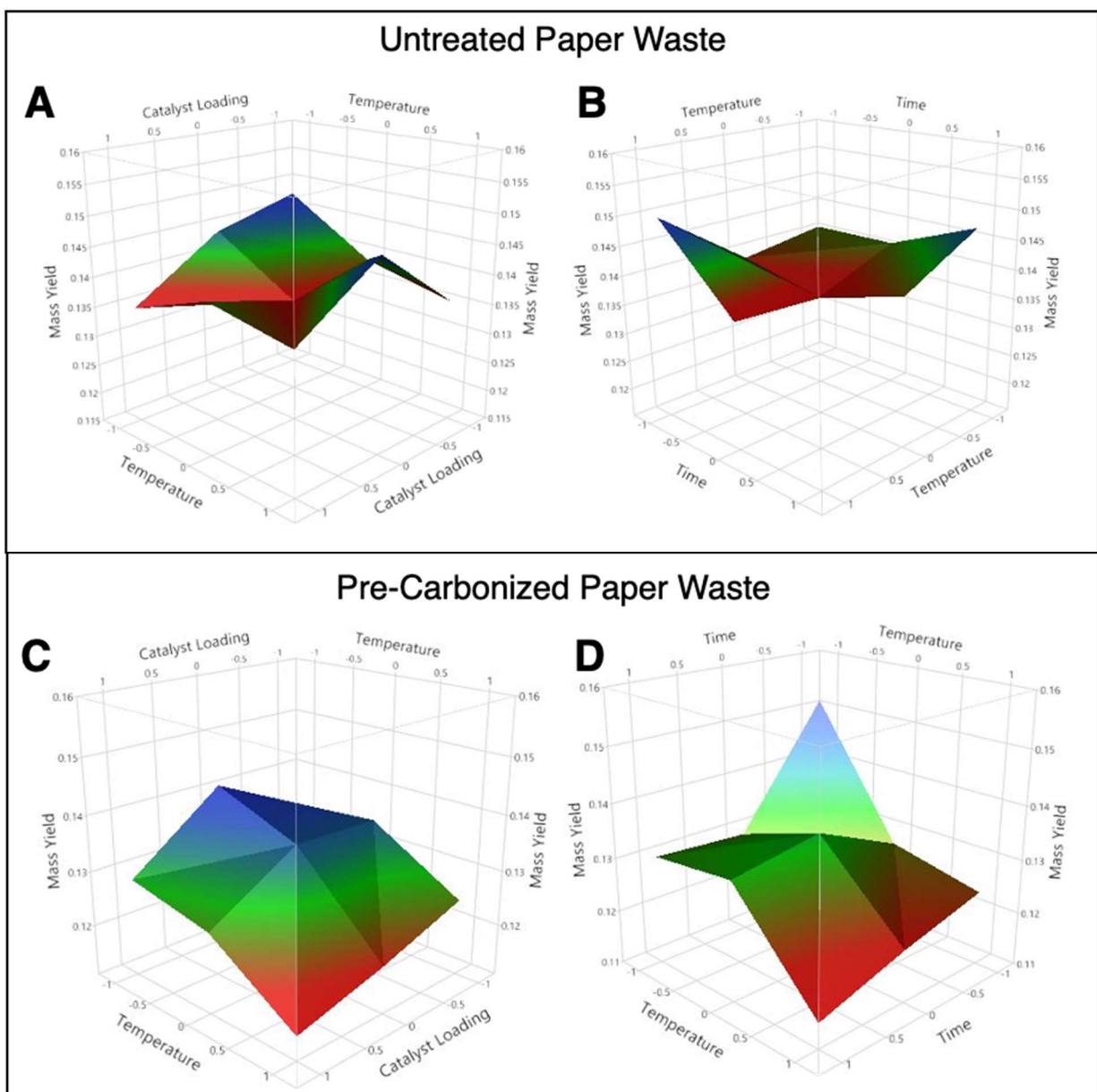


**Figure 1.2:** Response surface plots with biographite mass yield on z-axis and temperature, catalyst loading, and time on x-axes. A) untreated PW biographite mass yield with variation in temperature and catalyst loading B) untreated PW biographite mass yield with variation in temperature and time, C) pre-carbonized PW biographite mass yield with variation in temperature and catalyst loading, D) pre-carbonized PW biographite mass yield with variation in temperature and time.

As shown in Figure 1.3, response surface plots were generated to visualize the relationship between biographite d-spacing and temperature, catalyst loading, and time. For untreated PW, low temperature and low catalyst loading very clearly results in a large d-spacing, indicated by the sharp blue maximum in plot 1.3.A. Interestingly, catalyst loadings of 0 and +1 for untreated PW provide similar d-spacings regardless of the temperature, indicated by the broad, flat red minimum in plot 1.3.A. In plot 1.3.B, the maximum d-spacing is located at low temperature and medium time, thereby indicating a complex relationship with d-spacing at low temperatures. At medium to high temperatures, the d-spacing is relatively unaffected by time, indicated by the broad, flow red minimum shown in Plot 1.3.B. For pre-carbonized PW, the most obvious observation is the large spacing achieved at low temperature and time, indicated by the sharp blue maximum in plot 1.3D. Overall, the d-spacing relationships for pre-carbonized PW appear to be more complex than for untreated PW. However, the range in d-spacings is significantly less for pre-carbonized than for untreated PW, and thus the complex relationships are deemed relatively unimportant.

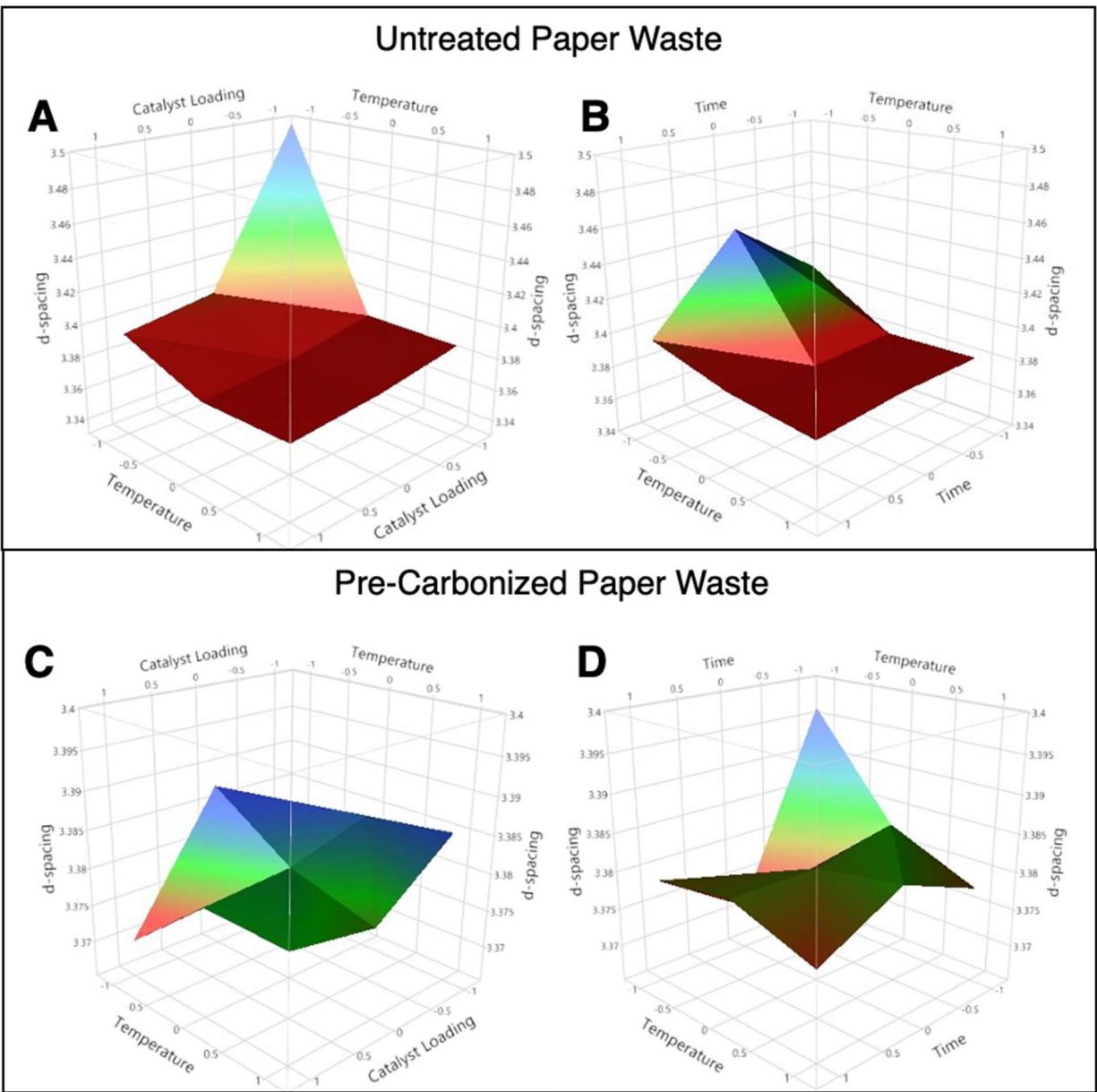


**Figure 1.3:** Response surface plots with biographite d-spacing on z-axis and temperature, catalyst loading, and time on x-axes. A) untreated PW biographite d-spacing with variation in temperature and catalyst loading B) untreated PW biographite d-spacing with variation in temperature and time, C) pre-carbonized PW biographite d-spacing with variation in temperature and catalyst loading, D) pre-carbonized PW biographite d-spacing with variation in temperature and time.

To further understand difference in graphite quality, the Degree of Disorder (DoD) was quantified for the maximum and minimum crystal sizes for untreated and pre-carbonized PW, as shown in Table 1.4. The low DoD values clearly correspond to high crystal sizes, and vice versa. Thus, DoD offers a new metric that is uniquely positioned to provide a quality assessment of biomass-derived carbon materials. Most biochar materials are disordered, and the quantification of crystal size via XRD is challenging and often inaccurate due to the broad and asymmetric peak. Thus, the DoD offers a simple method for quantifying disorder. From this study, it appears that DoD values greater than 2 are highly disordered, thereby making this a threshold value moving forward. Future work should investigate relationships between DoD and electrochemical performance in batteries.

**Table 1.4:** *Maximum and Minimum Crystal Size and Degree of Disorder Comparison*

	<b>Crystal Size</b>	<b>DoD</b>
Untreated	33.06	2.34
	91.05	0.92
Pre-Carbonized	43.73	2.06
	85.27	1.09

A statistical analysis was conducted to identify the significance or insignificance of various factors and combinations of factors for biographite crystal size, as shown in Table 1.5. Based on prior work by our group, biographite crystal size was deemed the most important response variable with regards to suitability in lithium-ion batteries, and was thereby selected for optimization. As shown in Table 1.5, temperature and catalyst loading were identified as significant for both untreated and pre-carbonized, whereas hold time was found to be

insignificant for both untreated and pre-carbonized. Overall, both statistical analyses show significant or moderately significant p-values and were therefore deemed acceptable for use in determining optimal graphitization conditions. The data from the Box Behnken design was interpreted by JMP statistical software to derive a multi-factorial optimization model, with the corresponding model p-values also shown in Table 1.5. The supporting information contains more information related to the multi-factorial models.

**Table 1.5:** *Results from the statistical analysis that was conducted to identify the significance or insignificance of various factors and combinations of factors for biographite crystal size (Significant  $p \leq 0.05$ , Moderately Significant  $p \leq 0.10$ , Insignificant  $p > 0.10$ )*

	<b><u>Untreated</u></b>	<b><u>Pre-Carbonized</u></b>
Temp	Significant	Significant
Catalyst Loading	Significant	Significant
Time	Insignificant	Insignificant
Temp <sup>2</sup>	Significant	Insignificant
Temp * Time	Moderately Significant	Insignificant
Temp <sup>2</sup> * Time	Significant	-
Temp * Catalyst Loading	-	Insignificant
Time <sup>2</sup>	Insignificant	Insignificant
Time * Catalyst Loading	Significant	Insignificant
Catalyst Loading <sup>2</sup>	Significant	Insignificant
<b>Model p-value</b>	<b>Significant</b>	<b>Moderately Significant</b>

The statistical models provided optimal levels and corresponding predicted graphite crystal sizes for both untreated and pre-carbonized PW, as shown in Table 1.5. To understand the accuracy of the statistical models, experiments were carried out using the optimal levels for each factor, with the resulting x-ray diffractograms, Rama spectra, and crystal sizes presented in Figure 1.4, Figure 1.5, and Table 1.5 respectively. Figure 1.4 shows the XRD patterns comparing

optimal graphite samples and commercial graphite. Qualitatively, the commercial graphite pattern demonstrates a narrower peak at two-theta of  $26^\circ$  and the characteristic peaks near two-theta of  $42^\circ$  are more distinct, relative the optimal biographite samples. Nonetheless, the XRD patterns of the biographite samples clearly indicate highly crystalline materials, particularly when compared to traditional biochar materials.

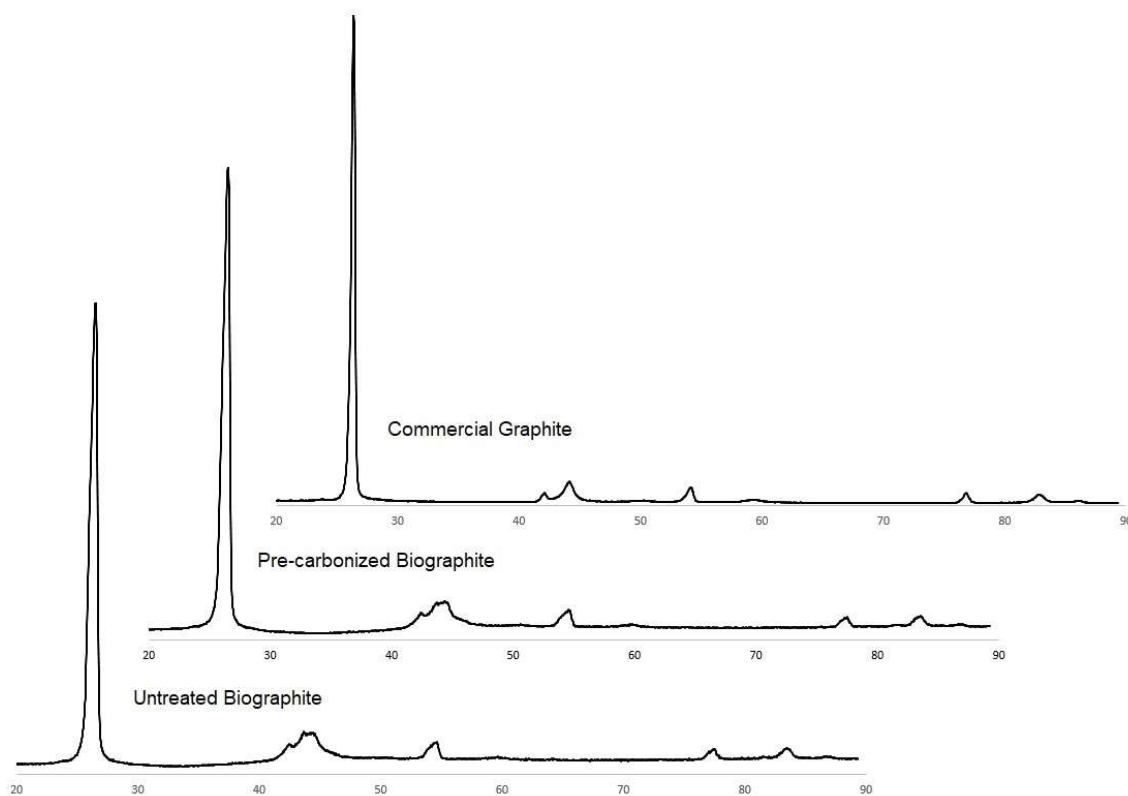


**Figure 1.4:** *X-ray diffractograms of commercial graphite, optimal pre-carbonized biographite, and optimal untreated biographite*

Extent of graphitization is another metric to compliment crystal size and degree of disorder to understand the quality of the biographite samples. Raman spectroscopy was used to quantify the extent of graphitization for the two optimal biographite samples, as shown in Figure

1.6. A series of 10 spectra were taken at different regions in each optimal biographite sample. For untreated PW biographite, the extent of graphitization was estimated to be 83.8% with a standard deviation of 9.34%. For pre-carbonized biographite, the extent of graphitization was calculated as 91.4% with a standard deviation of 4.19%. Thus, biographite resultant from pre-carbonization exhibits more uniform graphitization with fewer regions of disorder.

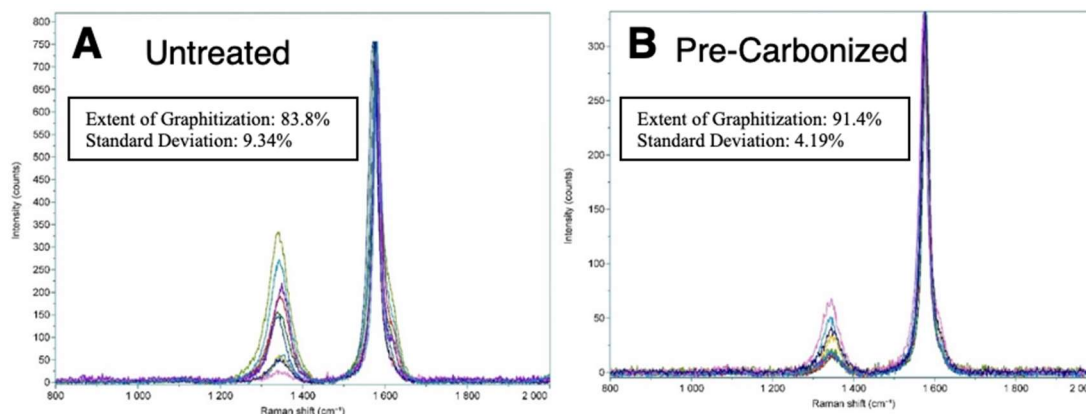


**Figure 1.5:** Raman spectra for A) untreated and B) pre-carbonized biographite

For pre-carbonized PW, the statistical model predicted a graphite crystal size of 79.46 angstroms with optimal levels of 1300°C, 1.88 hour, and 1.5X fixed carbon iron loading. The actual crystal size obtained was 80.17 angstroms, which is 100.89% of predicted value and therefore demonstrates high efficacy of the statistical model. For untreated PW, the statistical model predicted a graphite crystal size of 95.88 angstroms with optimal levels of 1243°C, 1-hour hold, and 1.5X fixed carbon iron loading. The actual crystal size obtained was 80.36 angstroms, which is 83.81% of predicted value and therefore demonstrates low efficacy of the statistical model. The poor efficacy of statistical model for untreated PW is thought to be due in-part to the relatively high standard deviation in extent of graphitization for untreated PW (9.34%), relative to pre-carbonized (4.19%). In addition, the volatile reactions that occur during graphitization with untreated PW might lead to relationships that are not captured by the statistical models.

**Table 1.6:** Optimal conditions for maximum crystal size and corresponding predicted and actual crystal size

Sample	Temperature (degree Celsius)	Hold Time (hour)	Catalyst Loading (catalyst: fixed carbon)	Predicted Crystal Size (Angstroms)	Actual Crystal Size (Angstroms)
Untreated	1243°C	1.0h	1.5	95.88	80.36
Pre-Carbonized	1300°C	1.9h	1.5	79.46	80.17

Finally, predictability is generally poor at the boundaries of levels in statistical models, which might also explain the relative inaccuracy of the statistical model. Figure 1.4 shows the prediction profile curves for both the untreated and pre-carbonized statistical models. In the untreated profile, Figure 1.4A, the optimal levels for time and catalyst loading are at the extreme ends (-1 for time and +1 for catalyst loading). In the pre-carbonized profile, Figure 1.4B, the optimal levels for temperature and catalyst loading are at the extreme ends (+1 for temperature and +1 for catalyst loading). Thus, future work should expand level boundaries to ensure the statistical models captures effects with higher accuracy.

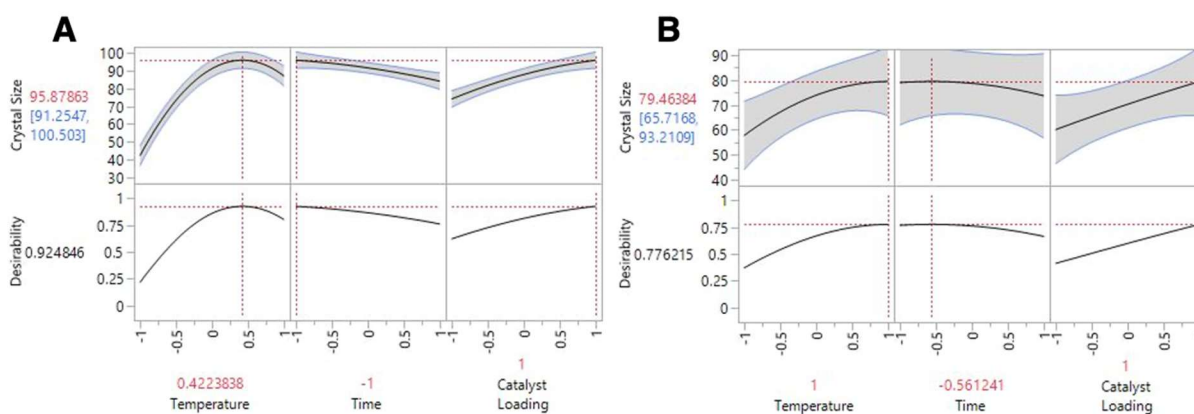


**Figure 1.6:** Statistical model prediction profiles for A) untreated and B) pre-carbonized

### 1.3.2 Mass Balance

To satisfy Objective 3, a thorough quantification of the mass composition of the various flows in the process were quantified and compared for the optimized untreated and pre-carbonized biographites. Elemental composition via scanning electron microscopy-energy dispersive X-ray spectroscopy (SEM-EDS) was corroborated with inductively-coupled plasma-optical emission spectrometry, CN macro determination, and thermogravimetric analysis. As shown in Table 1.7, the untreated PW feedstock contained calcium at higher levels than expected, likely due to the use of precipitated calcium carbonate in the paper towel product to enhance whiteness<sup>42,43</sup>. Fortunately, calcium is an ion that readily reacts with hydrochloric acid and was efficiently removed during the purification step as expected<sup>44</sup>. Silicon, however, is an element that does not dissolve in the presence of HCl, hence why it's still present in the final graphite product after purification<sup>45</sup>. Notably, the small amount presence of silicon left in the graphite might actually enhance electrochemical performance since the electron storage capacity of silicon is 800% greater than graphite<sup>46</sup>. Silicon significantly swells in size upon electron loading, hence why it must be used in small loadings<sup>47</sup>. Recent reports indicate that Tesla Motors dopes their graphite battery anodes with small quantities of silicon, and thus perhaps the naturally occurring silicon on the PW feedstock could serve as a benefit in battery performance<sup>48</sup>. Research is being performed looking at the use of silicon flakes coated in a carbon structure in addition to doping carbon nanotubes with silicon as possible anode alternatives<sup>49,50</sup>. Residual iron and chlorine from the purification process constitute approximately 0.3 – 0.4% of the final graphite product, and thus further improvements in purification are required. Nonetheless, the reduction in iron content is significant, decreasing from the intermediate compositions of 29.1% and 17.0% to 0.2% in the final graphite products

for the untreated and pre-carbonized samples, respectively. The oxygen contents in pre-carbonized intermediate and biographite were unexpected and warrant further investigation in future work. Battery-grade graphite typically requires carbon purity of greater than 99.9% to achieve high electrochemical performance, and thus it initially appeared that the biographite samples would perform poorly in battery cell testing. However, the biographite materials exceeded expectations as will be explained further in subsequent sections.

**Table 1.7: Mass Composition**

	Untreated			Pre-Carbonized		
	Feedstock	Intermediate	Graphite	Feedstock	Intermediate	Graphite
Carbon	51.8%	69.7%	99.3%	92.3%	78.4%	96.5%
Oxygen	47.0%	-	-	5.3%	3.8%	2.6%
Iron	-	29.1%	0.2%	-	17.0%	0.2%
Calcium	0.6%	0.8%	-	0.9%	0.3%	-
Silicon	0.1%	0.1%	0.3%	0.2%	0.1%	0.3%
Chlorine	-	-	0.1%	-	-	0.2%
Other	0.5%	0.3%	0.1%	1.3%	0.4%	0.2%

As shown in Figure 1.7, the final graphite yields for untreated and pre-carbonized were 14.27g and 13.4g, respectively, starting with 100g of dry, untreated PW. The optimal catalyst loading was determined to be 27.4g of iron per 100g of dry, untreated PW, of which approximately 2.5g is lost during graphitization and the remainder removed during HCl purification. The high iron loading is justified due to the use of low-cost, iron shaving residue readily available at steel mills (further discussion in the subsequent section on techno-economics). The ~2.5g of iron lost during graphitization is likely due to violent reactions between small iron particles (<1 um) and volatilized carbon. As can be seen in the pre-carbonized process flow diagram, approximately 25% of the mass of the pre-carbonized PW is lost during graphitization, thereby indicating the

iron induces some increased reactivity and volatility. Also, the nitrogen gas flow was likely sufficiently high to carry lightweight, low density particles out of the crucible. In future work, the volatilized mass needs to be analyzed to fully close the mass balance. Herein, the mass balance was closed by deduction, which was possible given that the mass via graphitization loss was the only unknown mass flow. The pre-carbonized process involves an extra step (pre-carbonization), but is likely a better approach for commercial production given that significantly less mass is required in the capital-intensive graphitization reactor, relative to the untreated process.

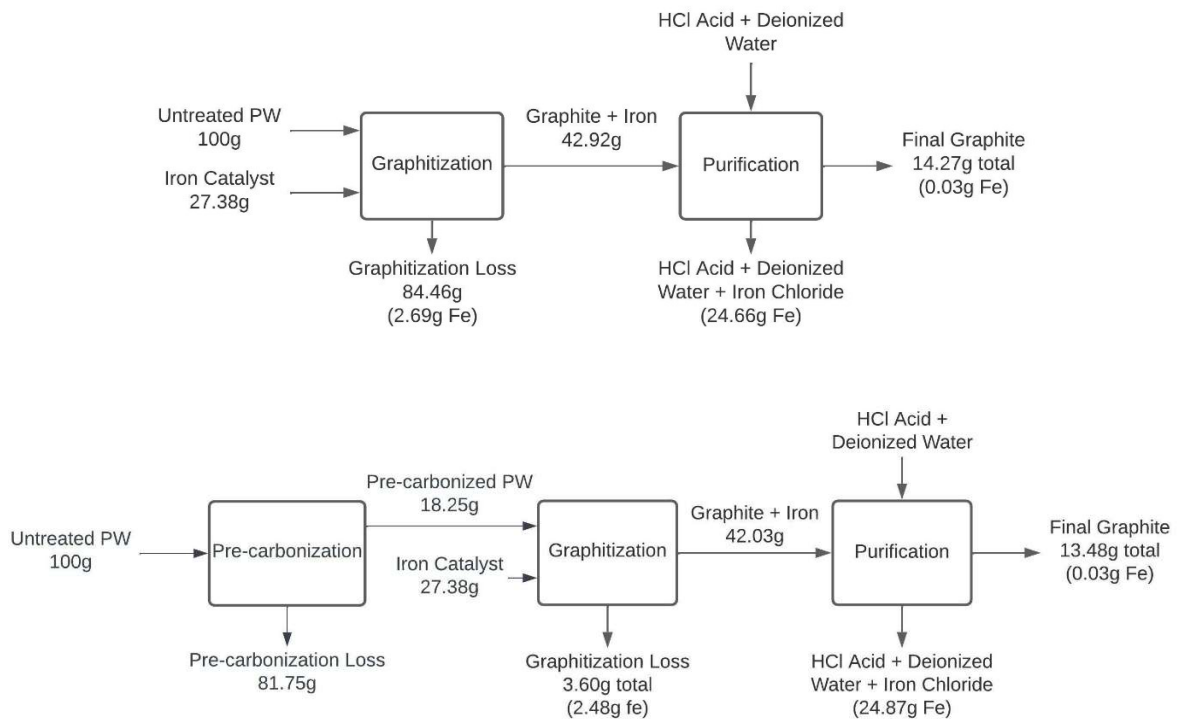


**Figure 1.7:** Mass balances for untreated (top) and pre-carbonized (bottom) paper waste

### 1.3.3 Biographite Morphology

To satisfy Objective 4, the biographite products were observed via SEM and TEM. Graphitic carbon morphologies typical of those reported in steel refining, including spheres, platelets, and cones<sup>51</sup>, were observed in our study. Unlike natural flake graphite and synthetic graphite from petroleum-derived needle coke, iron-catalyzed graphite contains crystalline regions of relatively small size in the a-direction and large size in the c-direction. This phenomena ultimately leads to a preferred spherical or conical morphology, since the graphite grows faster in the c-direction rather than the a-direction. As shown in Figures 1.8 and 1.9, both conical and spherical morphologies are observed from untreated and pre-carbonized graphite products, respectively<sup>20,31</sup>. Notably, uniform distribution of the iron throughout the PW cellulose fibers was observed in the EDS images of both untreated and pre-carbonized biographite, as shown in Figures 1.8 and 1.9. Therefore, the relatively simple method of dry mixing the iron powder catalyst with the PW particles appears to be sufficient in providing uniform distribution of catalyst throughout the biocarbon, although the distribution could likely be improved for the untreated PW per the relatively poor extent of graphitization.

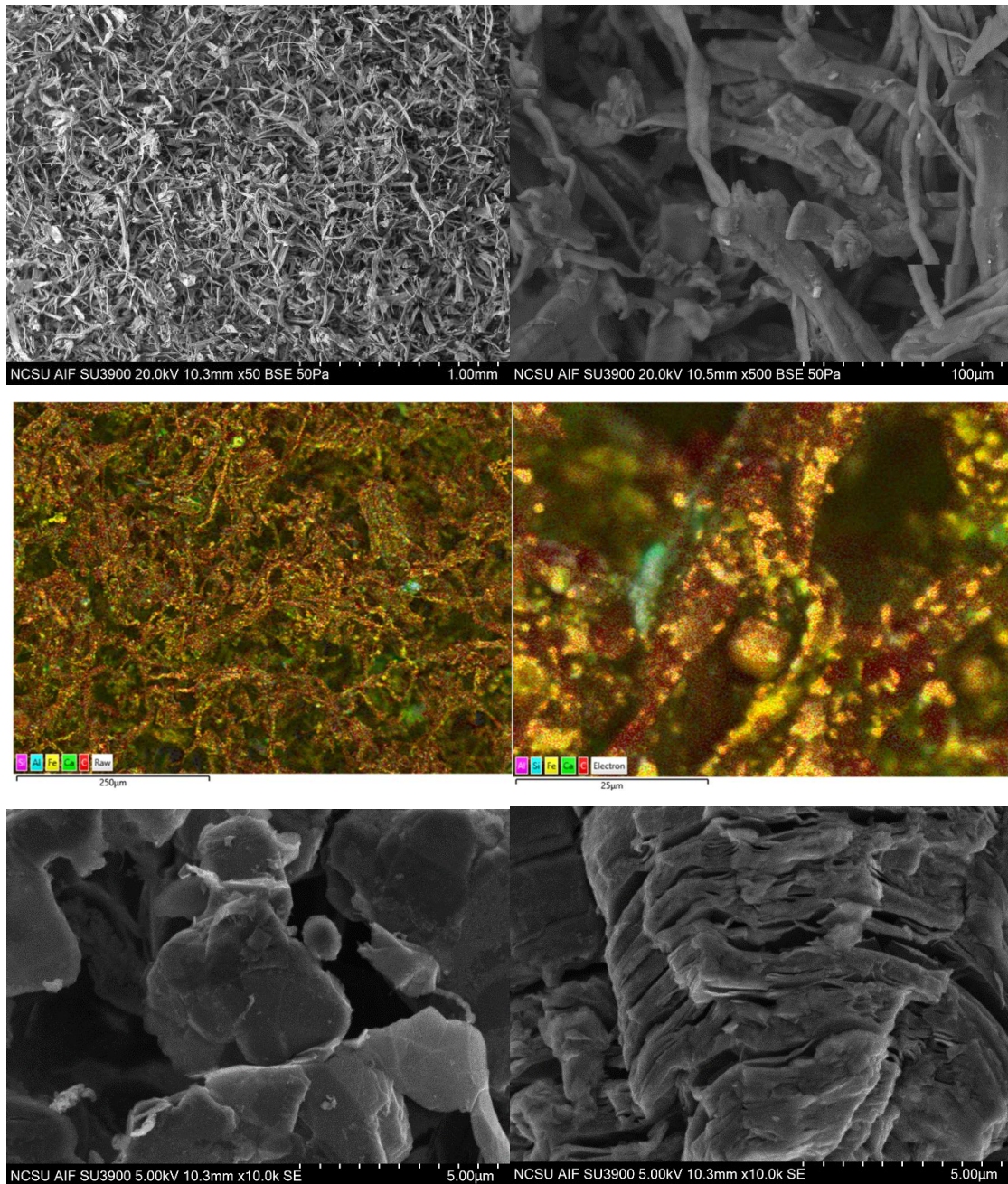


**Figure 1.8:** SEM Images of Untreated PW (top), EDS Images of Untreated Graphite with Iron (middle), and Untreated Graphite SEM (bottom)

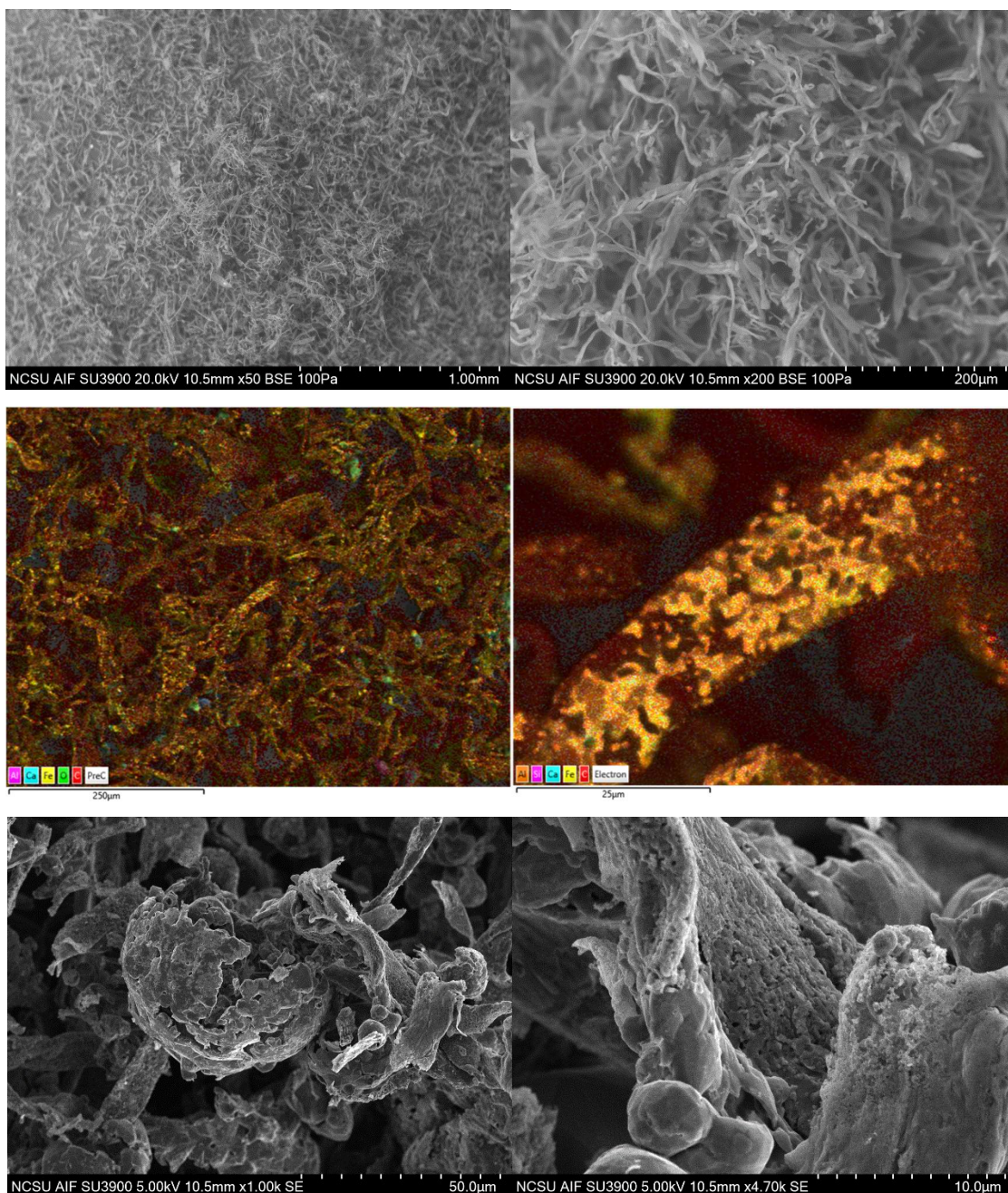


**Figure 1.9:** SEM Images of Pre-carbonized PW (top), EDS Images of Graphite with Iron (middle), and SEM Images of Pre-carbonized Graphite (bottom)

In addition to micron-level imaging via SEM, nano-level imaging via TEM was conducted, wherein individual layers of graphitic carbon were observed<sup>32,33</sup>, as shown in Figure

1.10. The mechanism of iron-catalyzed graphitization involves solubilization of disordered carbon in molten eutectic iron until saturation, at which point the carbon precipitates out of the iron solution in the form of graphite<sup>29</sup>. As seen in Figure 1.10, the graphite layering extends approximately 8 – 10 nm (80 – 100 angstrom), thereby corroborating the  $L_c$  values quantified via XRD and reported in Table 1.6.

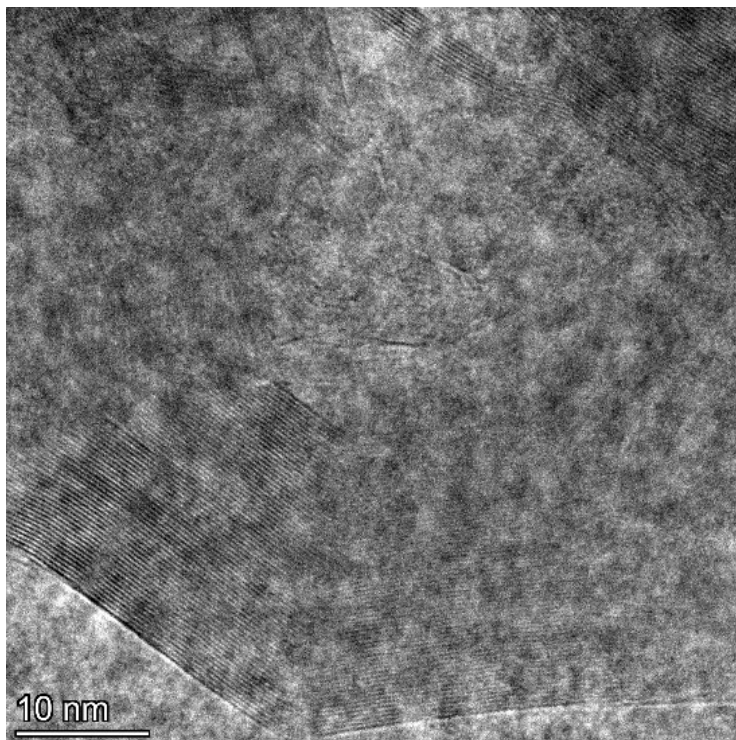


**Figure 1.10:** *TEM Image of Untreated Graphite*

### **1.3.4 Lithium-Ion Cell Performance**

To satisfy Objective 5, the biographite products were used in the construction of lithium-ion half cells for galvanostatic discharge and charge cycling. The reversible capacities (at C/10 in the voltage range of 0.005 - 1.5 V) of our untreated graphites and pre-carbonized graphites are approximately 355 and 340 mAh g<sup>-1</sup>, respectively, indicating great electrochemical performance of the synthesized materials based on theoretical capacity (372 mAh g<sup>-1</sup> by forming intercalation

compounds  $\text{LiC}_6$ ) of graphite (Figure 1.11). The initial Coulombic efficiency (CE) of both graphites, however, is 76.2% (average value of four cells)—less than the typical commercial graphite CE of 92-94%—suggesting severe parasitic reactions (e.g., electrolyte decomposition and lithium inventory loss) during the first discharging possibly due to the morphology, high surface area and surface reactivity of bio graphite particles. Typically, initial low CE results in poor cyclability in a full cell (finite lithium inventory from cathode and electrolyte), so it should be improved by employing possible strategies, such as surface modification and size and morphology control of particles. The initial capacity loss is also due to a solid-electrolyte interphase (SEI) layer forming<sup>52</sup>, and significant increase of CE (97%) for the 2<sup>nd</sup> cycle and stable CE values for the subsequent cycles suggest formation of stable SEI layers on graphite anodes.

Cycling stability tests are performed comparing the untreated, pre-carbonized, and commercial graphite samples (Figure 1.11b). Through the first 27 cycles the materials all show great promise as anode material for lithium-ion batteries. More cycles are being performed and a full cyclability test (up to 100 cycles) will be completed. The rate ability of the PW graphite is tested to determine the reversible  $\text{Li}^+$  ion intercalation and de-intercalation behaviors at various C-rates, which is shown in Figure 1.11c. The graphite shows a relatively large capacity reduction with any C-rate over 1.0C, but still the reversible capacities at higher C-rates demonstrate much higher values than those of our previous graphite materials<sup>20</sup>. In addition, the graphite sample shows amazing capacity recovery when the C-rate is brought back down to 0.1C, recovering to initial capacity. Finally, as shown in Figure 1.11, the untreated (raw) PW biographite is performing slightly better than pre-carbonized for reasons that are currently unclear. Possible reasons for the discrepancy in electrochemical performance between the two biographite

materials might due to the slight difference in graphite crystal sizes or, more likely, the increased levels of non-carbon impurities in the pre-carbonized biographite. Moving forward, improvements in purification of the pre-carbonized biographite should enhance electrochemical performance.

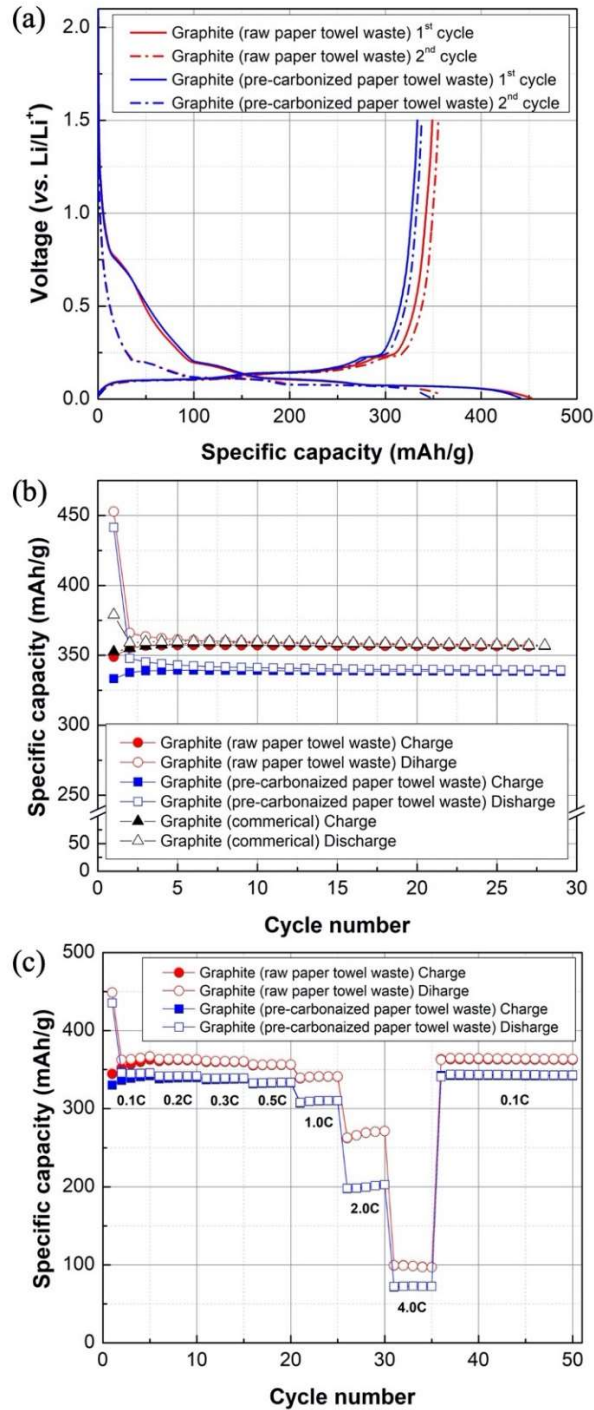


**Figure 1.11:** Electrochemical performance of bio graphites (from paper towel waste): (a) galvanostatic discharge and charge profiles and (b) cycling stability plot (commercial graphite for comparisons) (at  $C/10$  in the voltage range of 0.005 - 1.5 V). (c) Rate capability plot (at varying  $c$ -rate in the voltage range of 0.005 - 1.5 V).

## 1.4 Conclusions

The catalytic graphitization of paper waste for use in Li-ion battery anodes was proven to be technically feasible through the successful completion of the five aforementioned objectives. Objective 1 was satisfied by identifying advantages and disadvantages to pre-carbonizing PW prior to graphitization. Pre-carbonizing the PW before catalytic graphitization resulted in greater center point consistency, relative to untreated PW. In addition, the range in crystal sizes, variation in d-spacing, and standard deviation of extent of graphitization are substantially lower for pre-carbonized than for untreated, thereby providing strong evidence for pre-carbonization as a more consistent, and reliable method for catalytic graphitization. The extent of graphitization for pre-carbonized biographite is also greater (91.4% vs. 83.8%), thereby reinforcing the claim that pre-carbonized biographite is a more complete and consistent biographite product. However, the maximum crystal size obtained with pre-carbonized PW was less than with untreated PW (85.3 vs. 95.1 angstroms), and was achieved at a considerably higher temperature (1300C vs. 1200C) and longer hold time (3h vs. 1h). Thus, untreated PW appeared to provide higher quality graphite at milder conditions, albeit with less uniformity than with pre-carbonization. For both untreated and pre-carbonized PW, the biographite yields were approximately the same (11 – 15%). For both untreated and pre-carbonized PW, the maximum crystal size was obtained with a high catalyst loading (1.5X fixed carbon), thereby confirming the importance of the iron catalyst. The minimum d-spacing for both untreated and pre-carbonized PW is approximately 3.37 angstroms, which is suitable for lithium-ion intercalation. Thus, the main advantage of pre-carbonization appears to be a more uniform graphite product with high extent of graphitization, while the disadvantages include a relatively low quality graphite and the requirement for relatively higher temperatures and longer hold times. The main advantages of using untreated

PW appears to be higher quality graphite and the requirement for relatively lower temperatures with shorter hold times, while the disadvantage is a less uniform and consistent graphite product. Although not within the scope of this study, there likely exists techno-economic advantages to pre-carbonization due to the lower volatility in the graphitization reactor, relative to directly processing untreated PW in the graphitization reactor.

To satisfy Objective 2, a statistical analysis was conducted to identify the significance or insignificance of various factors and combinations of factors for biographite crystal size. Temperature and catalyst loading were identified as significant for both untreated and pre-carbonized, whereas hold time was found to be insignificant for pre-carbonized and untreated but close to the moderately significant threshold. However, at lower temperatures there was a noticeable increase in crystal size with longer time, indicating graphitization could be occurring at a slower rate. Overall, both statistical analyses show significant or moderately significant p-values and were therefore deemed acceptable for use in determining optimal graphitization conditions. The statistical model for the pre-carbonized biographite was highly accurate, whereas that for the untreated biographite demonstrated inaccuracy. The poor efficacy of the statistical model for untreated PW is thought to be due in-part to the relative non-uniformity in the graphite product. In addition, the volatile reactions that occur during graphitization with untreated PW might lead to factor relationships that are not captured by the statistical models. Notably, the statistical models determined the optimal levels for both untreated and pre-carbonized PW to be at the extreme ends of the bounds, and thus further enhancement in graphite quality and statistical model performance seems possible with expanded bounds.

To satisfy Objective 3, a thorough quantification of the mass composition of the various flows in the process were quantified and compared for the optimized untreated and pre-

carbonized biographites. The overall mass yields were 14.27% and 13.48% for untreated and pre-carbonized PW under optimal graphitization conditions, respectively. Typically, high mass yields were accompanied by low graphite crystal size, and thus mass yield should not necessarily be optimized at the expense of crystal size. Hydrochloric acid is highly effective at removing the iron catalyst and other cations, such as calcium. Silica is not highly soluble in hydrochloric acid, and thus residual exists in the biographite product. Notably, the residual silica might enhance electrochemical performance and warrants further attention. In addition, the oxygen contents in the intermediate and final biographite products from pre-carbonized PW deserve further investigation. From a techno-economic perspective, the pre-carbonized process involves an extra step (pre-carbonization), but is likely a better approach for commercial production given that significantly less mass is required in the capital-intensive graphitization reactor, relative to the untreated process.

To satisfy Objective 4, the morphologies of the biographite products were observed and analyzed. Graphitic carbon morphologies typical of those reported in steel refining, including spheres, platelets, and cones<sup>51</sup>, were observed in our study. The mechanism of iron-catalyzed graphitization involves solubilization of disordered carbon in molten eutectic iron until saturation, at which point the carbon precipitates out of the iron solution in the form of graphite<sup>29</sup>. Due to the similarity in graphite formation mechanisms, there exists the potential to incorporate intentional graphitization into the steel refining process. Notably, uniform distribution of the iron throughout the PW biocarbon was observed in both untreated and pre-carbonized intermediate biographites, thereby confirming the efficacy of using a relatively simple method for dry mixing the iron powder catalyst.

To satisfy Objective 5, the biographite products were used in the construction of lithium-ion half cells for galvanostatic discharge and charge cycling. The electrochemical performance exhibited SEI formation and impressive CE after the first cycle. The reversible capacities (at C/10 in the voltage range of 0.005 - 1.5 V) of the untreated and pre-carbonized biographite were calculated to be 355 and 340 mAh g<sup>-1</sup>, respectively, which is highly competitive with commercial lithium-ion anodes. The biographite samples appear to have good cycling stability through the first 27 cycles and are initially promising. The untreated PW biographite is performing slightly better than pre-carbonized for reasons that are currently unclear. Possible reasons for the discrepancy in electrochemical performance between the two biographite materials might be due to the slight difference in graphite crystal sizes or, more likely, the increased levels of non-carbon impurities in the pre-carbonized biographite. Moving forward, improvements in purification of the pre-carbonized biographite should enhance electrochemical performance. The developed biographite Li-ion batteries appear to be more suitable for grid level storage with relatively slow charge and discharge rates, and less suitable for fast-charging batteries in personal devices or electric vehicles.

To satisfy Objective 6, the following actions are recommended in future work. Expand the boundaries of temperature and catalyst loading since the statistical models found optimal points to be near the extremes. Although not captured by the statistical models, observations indicate that significantly longer hold times at relatively low temperatures might produce a high quality biographite, and thus warrant consideration. The relatively high presence of oxygen in the final pre-carbonized biographite product and its effect on electrochemical performance needs to be understood. Alternative methods of iron removal, such as selective oxidation of iron and diamagnetic separation, should be explored. In addition, the effect of residual silica on

electrochemical performance must be elucidated, particularly given that silica is currently used as a dopant in commercial graphite anodes. A thorough techno-economic assessment comparing pre-carbonization and untreated methods of production must be conducted. Finally, a feasibility assessment of integrating biographite synthesis and separation in existing blast furnace-basic oxygen furnace steel refining operations should be considered.

## REFERENCES

1. Romare, M. & Dahllöf, L. The Life Cycle Energy Consumption and Greenhouse Gas Emissions from Lithium-Ion Batteries A study with focus on Current Technology and batteries for high-duty vehicles. *IVL Swedish Environmental Research Institute* (2017).
2. Lewis, M. Graphite will be in deficit from 2022 – here 's what EV battery makers need to do to secure the critical mineral. *Electrek* <https://electrek.co/2021/12/20/graphite-will-be-in-deficit-from-2022-heres-what-ev-battery-makers-need-to-do-to-secure-the-critical-mineral/> (2022).
3. Chehreh Chelgani, S., Rudolph, M., Kratzsch, R., Sandmann, D. & Gutzmer, J. A Review of Graphite Beneficiation Techniques. *Miner. Process. Extr. Metall. Rev.* **37**, 58–68 (2016).
4. Mayyas, A. Are there enough materials to cover li- ion batteries? *National Renewable Energy Laboratory* (2018).
5. Olivetti, E. A., Ceder, G., Gaustad, G. G. & Fu, X. Lithium-Ion Battery Supply Chain Considerations: Analysis of Potential Bottlenecks in Critical Metals. *Joule* **1**, 229–243 (2017).
6. Whiteside, J. & Finn-Foley, D. Supply Chain Looms as Serious Threat to Batteries' Green Reputation. *Wood Mackenzie* (2019).
7. Pierson, H. *Handbook of carbon, graphite, diamond and fullerenes*. (Noyes Publications, 1993).
8. Dahn, J. R., Zheng, T., Liu, Y. & Xue, J. S. Mechanisms for Lithium Insertion in Carbonaceous Materials. *Science (80-. )*. **270**, 590–594 (1995).
9. Jara, A. D., Betemariam, A., Woldetinsae, G. & Kim, J. Y. Purification, application and

- current market trend of natural graphite: A review. *Int. J. Min. Sci. Technol.* **29**, 671–689 (2019).
10. Dunn, J. B., Gaines, L., Barnes, M., Wang, M. & Sullivan, J. Material and energy flows in the materials production, assembly, and end-of-life stages of the automotive lithium-ion battery life cycle. *Argonne Natl. Lab* (2014).
  11. Sawarkar, A. N., Pandit, A. B., Samant, S. D. & Joshi, J. B. Via Delayed Coking : A Review. *Can. J. Chem. Eng.* **85**, (2007).
  12. Truong, C. N. *et al.* Economics of residential photovoltaic battery systems in Germany: The case of tesla's powerwall. *Batteries* **2**, (2016).
  13. Bogdanov, D. *et al.* Radical transformation pathway towards sustainable electricity via evolutionary steps. *Nat. Commun.* **10**, 1–16 (2019).
  14. Crabtree, G. The coming electric vehicle transformation. *Science (80-. )*. **366**, 422–424 (2019).
  15. Dunn, J. B. *et al.* Material and energy flows in the production of cathode and anode materials for lithium ion batteries. *Argonne Natl. Lab.(ANL) ANL/ESD-14*, 68–70 (2015).
  16. Manthiram, A. An Outlook on Lithium Ion Battery Technology. *ACS Cent. Sci.* **3**, 1063–1069 (2017).
  17. Franklin, R. E. Crystallite growth in graphitizing and non-graphitizing carbons. *Proc. R. Soc.* **209**, 196–218 (1951).
  18. Sagues, W. J. *et al.* Are lignin-derived carbon fibers graphitic enough? *Green Chem.* **21**, 4253–4265 (2019).
  19. Liedel, C. Sustainable Battery Materials from Biomass. *ChemSusChem* **13**, 2110–2141 (2020).

20. Sagues, W. J. *et al.* A simple method for producing bio-based anode materials for lithium-ion batteries. *Green Chem.* 7093–7108 (2020) doi:10.1039/d0gc02286a.
21. Li, J., Daniel, C. & Wood, D. Materials processing for lithium-ion batteries. *J. Power Sources* **196**, 2452–2460 (2011).
22. Noda, S. & Yamaguchi, Y. Estimation of surface iron oxide abundance with suppression of grain size and topography effects. *Ore Geol. Rev.* **83**, 312–320 (2017).
23. United States Environmental Protection Agency. Nondurable Goods: Product-Specific Data. Overview of Nondurable Goods. <https://www.epa.gov/facts-and-figures-about-materials-waste-and-recycling/nondurable-goods-product-specific-data> (2021).
24. Kool, T. Why Graphite Could Be The Hottest Commodity Of 2022. *FN Media Group* (2022).
25. Joseph, T., Baah, K., Jahanfar, A. & Dubey, B. A comparative life cycle assessment of conventional hand dryer and roll paper towel as hand drying methods. *Sci. Total Environ.* **515–516**, 109–117 (2015).
26. Argun, H. & Onaran, G. Hydrogen gas production from waste paper by sequential dark fermentation and electrohydrolysis. *Int. J. Hydrogen Energy* **41**, 8057–8066 (2016).
27. Dutta, S. *et al.* Influence of green solvent on levulinic acid production from lignocellulosic paper waste. *Bioresour. Technol.* **298**, 122544 (2020).
28. Reynolds, K. A., Sexton, J. D., Norman, A. & McClelland, D. J. Comparison of electric hand dryers and paper towels for hand hygiene: a critical review of the literature. *J. Appl. Microbiol.* **130**, 25–39 (2021).
29. Thompson, E., Danks, A. E., Bourgeois, L. & Schnepf, Z. Iron-catalyzed graphitization of biomass. *Green Chem.* **17**, 551–556 (2015).

30. Zhou, X. *et al.* Interconnected highly graphitic carbon nanosheets derived from wheat stalk as high performance anode materials for lithium ion batteries. *Green Chem.* **18**, 2078–2088 (2016).
31. Banek, N. A., Abele, D. T., McKenzie, K. R. & Wagner, M. J. Sustainable Conversion of Lignocellulose to High-Purity, Highly Crystalline Flake Potato Graphite. *ACS Sustain. Chem. Eng.* **6**, 13199–13207 (2018).
32. Gomez-Martin, A. *et al.* Iron-Catalyzed Graphitic Carbon Materials from Biomass Resources as Anodes for Lithium-Ion Batteries. *ChemSusChem* **11**, 2776–2787 (2018).
33. Gomez-Martin, A. *et al.* Porous Graphene-like Carbon from Fast Catalytic Decomposition of Biomass for Energy Storage Applications. *ACS Omega* **4**, 21446–21458 (2019).
34. Fromm, O. *et al.* Carbons from biomass precursors as anode materials for lithium ion batteries: New insights into carbonization and graphitization behavior and into their correlation to electrochemical performance. *Carbon N. Y.* **128**, 147–163 (2018).
35. Ōya, A. & Marsh, H. Phenomena of catalytic graphitization. *J. Mater. Sci.* **17**, 309–322 (1982).
36. Xia, S. *et al.* Synthesis and formation mechanism of biomass-based mesoporous graphitic carbon. *Fuel Process. Technol.* **209**, 106543 (2020).
37. Hong, S. J., Kim, S. S. & Nam, S. Using coffee-derived hard carbon as a cost-effective and eco-friendly anode material for li-ion batteries. *Corros. Sci. Technol.* **20**, 15–21 (2021).
38. Xie, A. *et al.* Hierarchical porous carbon materials derived from a waste paper towel with ultrafast and ultrahigh performance for adsorption of tetracycline. *RSC Adv.* **6**, 72985–72998 (2016).

39. Esteves, G., Ramos, K., Fancher, C. M., and Jones, J. L. LIPRAS: Line-Profile Analysis Software. (2017) doi:<https://doi.org/10.13140/RG.2.2.29970.25282/3>.
40. United States Environmental Protection Agency. *Acid Digestion of Sediments, Sludges, and Soils Method 3050B. Hazardous Waste Test Methods / SW-846* vol. 3050B (1996).
41. Xu, B., Wu, M. S., Liu, G. & Ouyang, C. Y. Understanding the effect of the layer-to-layer distance on Li-intercalated graphite. *J. Appl. Phys.* **111**, (2012).
42. Mohamadzadeh-Saghavaz, K., Resalati, H. & Ghasemian, A. Cellulose-precipitated calcium carbonate composites and their effect on paper properties. *Chem. Pap.* **68**, 774–781 (2014).
43. Lourenço, A. F., Gamelas, J. A. F., Sequeira, J., Ferreira, P. J. & Velho, J. L. Improving paper mechanical properties using silica-modified ground calcium carbonate as filler. *BioResources* **10**, 8312–8324 (2015).
44. Mulopo, J., Mashego, M. & Zvimba, J. N. Recovery of calcium carbonate from steelmaking slag and utilization for acid mine drainage pre-treatment. *Water Sci. Technol.* **65**, 2236–2241 (2012).
45. Yu, Z. *et al.* Kinetics of iron removal from metallurgical grade silicon with pressure leaching. *Rare Met.* **30**, 688–694 (2011).
46. Zhang, X., Kong, D., Li, X. & Zhi, L. Dimensionally Designed Carbon–Silicon Hybrids for Lithium Storage. *Adv. Funct. Mater.* **29**, 1–24 (2019).
47. Jin, D. *et al.* Highly Stabilized Silicon Nanoparticles for Lithium Storage via Hierarchical Carbon Architecture. *ACS Appl. Energy Mater.* **3**, 4777–4786 (2020).
48. Ruan, D. *et al.* A low-cost silicon-graphite anode made from recycled graphite of spent lithium-ion batteries. *J. Electroanal. Chem.* **884**, (2021).

49. Tzeng, Y., Chen, R. & He, J. L. Silicon-based anode of lithium ion battery made of nano silicon flakes partially encapsulated by silicon dioxide. *Nanomaterials* **10**, 1–13 (2020).
50. Zeferino González, I., Chiu, H. C., Gauvin, R., Demopoulos, G. P. & Verde-Gómez, Y. Silicon doped carbon nanotubes as high energy anode for lithium-ion batteries. *Mater. Today Commun.* **30**, (2022).
51. Ștefănescu, D. M., Alonso, G., Larrañaga, P., de La Fuente, E. & Suárez, R. Reassessment of Crystal Growth Theory of Graphite in Cast Iron. *Mater. Sci. Forum* **925**, 36–44 (2018).
52. Gnanaraj, J. S., Thompson, R. W., Iaconatti, S. N., Dicarolo, J. F. & Abraham, K. M. Formation and growth of surface films on graphitic anode materials for Li-ion batteries. *Electrochem. Solid-State Lett.* **8**, (2005).